Biophysical Chemistry 30 (1988) 3–48
Elsevier

BPC 01243

Review

Low-frequency collective motion in biomacromolecules and its biological functions

Kuo-Chen Chou

Computational Chemistry, Upjohn Research Laboratories, Kalamazoo, MI 49001, U.S.A.

Received 1 June 1987
Revised manuscript received 12 January 1988
Accepted 12 January 1988

Low-frequency resonance; DNA-drug intercalation; Hemoglobin; Cooperativity; Free energy deficit; Phonon entropy; Antibody; Trigger effect; Quasi-continuity model

The occurrence of low-frequency motion in biomacromolecules, which had long been speculated upon with a great deal of skepticism, is now a clearly established phenomenon and has been convincingly demonstrated. The next stage in the process of its elucidation appropriately concerns the determination of its origin, the development of a feasible and effective model for the calculations involved and, more importantly, the extending of investigations on its biological roles in order to gain insights into the various interesting mechanisms underlying the dynamic processes occurring in biomacromolecules. Confronted with such a task, this review has been written with the aim of stimulating further, through a systematic and comprehensive description, developments to open up this exciting frontier of molecular biology, especially from the viewpoint of biological functions.

1. Low-frequency internal motion

1.1. An interesting 'deficit' in free energy

At the outset, it is instructive to consider the thermodynamic relation for the following reaction

$$I + R \rightleftharpoons IR \tag{1}$$

where I denotes insulin, R the insulin receptor and IR the associated complex. According to experiments [1], the free energy for the above reaction is $\Delta G = -12$ kcal/mol. However, it is well known that, when two such molecules bind together, there is a loss of three translational degrees of freedom and of three rotational degrees of freedom, resulting in a loss of translational entropy (ΔS_{tran}) and of rotational entropy (ΔS_{rot}). Therefore, the free energy for eq. 1 can be written as

$$\Delta G = -T(\Delta S_{tran} + \Delta S_{rot}) + \Delta G^* \tag{2}$$

where ΔG^* is the contribution of all other factors to the free energy of association. The quantities ΔS_{tran} and ΔS_{rot} can be calculated, yielding $T(\Delta S_{tran} + \Delta S_{rot}) = -30$ kcal/mol at $T = 300$ K [2]. Substituting this quantity as well as $G = -12$ kcal/mol [1] into eq. 2, we obtain $\Delta G^* = -42$ kcal/mol, which is quite a large negative quantity. The problem which is thus presented concerns how such a large value of the free energy can be attained, or the establishing of the source from which ΔG^* originates. It is well known that when insulin and insulin receptor become associated with each other, no covalent bond is formed, only

Correspondence address: K.-C. Chou, Computational Chemistry, Upjohn Research Laboratories, Kalamazoo, MI 49001, U.S.A.

weak bonds such as hydrogen bonds and van der Waals bonds being involved. However, the weak bonds here do not make significant contribution to the free energy [3]. As a matter of fact, the experimental value of the enthalpy for association between insulin and insulin receptor is $\Delta H = -2$ kcal/mol [1], clearly indicating that intermolecular bonds contribute only very slightly to ΔG^*. Fortunately, there is a speical interaction, the so-called hydrophobic interaction, which has played an important role in the understanding of many phenomena concerning the interactions of biological macromolecules. Let us now consider the consequences of taking the hydrophobic interaction into account. It is known that 1 Å^2 of a protein-accessible hydrophobic surface [3] contributes -25 cal of free energy when such an area is buried within a protein after being originally exposed to water molecules [3]. On this basis, it was found that the hydrophobic interaction would contribute a free energy of $\Delta G_{\text{hydro}} \simeq -32$ kcal/mol [2] to the binding reaction between insulin and insulin acceptor. Nevertheless, as shown in the following equation

$$\begin{matrix} \Delta G^* & = & \Delta H & + \Delta G_{\text{hydro}} + & ? \\ (-42) & & (-2) & (-32) & (-8) \end{matrix} \tag{3}$$

there still remains a free energy of about -8 kcal/mol that cannot be balanced. We term such an unbalanced quantity a 'deficit'.

A similar deficit also occurs for the binding reaction between insulin and insulin antibody [2].

This at first appears to be very puzzling. However, on checking the above thermodynamic analysis carefully, a mistake resulting from negligence becomes evident. The pitfall is that although three translational and three rotational degrees of freedom are lost after binding of the two molecules, it may be forgotten that six vibrational degrees of freedom are generated simultaneously. This type of contribution is easily overlooked, unless the frequencies of these vibrational degrees of freedom are very low, since the entropy effects resulting thereby are extremely small and can be safely omitted. Only when the frequencies are at least two orders of magnitude lower than those found in ordinary molecules, do the vibrational entropy effects become conspicuous. This point will be further illustrated in section 1.2.

1.2. Entropy effects of low-frequency phonons

As is well known, an oscillator with frequency ν will excite phonons, each of energy $h\nu$, where h is Planck's constant. Since phonons fall within the category of bosons [4], at thermal equilibrium, the mean number $\langle n \rangle$ of phonons thus excited can be described by Bose-Einstein statistics; i.e.

$$\langle n \rangle = \frac{1}{e^{(h\nu-\mu)/k_B T} - 1}\bigg|_{\mu=0} = \frac{1}{e^{h\nu/k_B T} - 1} \tag{4}$$

where k_B is Boltzmann's constant, T the absolute temperature, and μ the chemical potential which is equal to zero in this case because the number of phonons is not conserved [4]. The energy of phonons created by 1 mol of such oscillators should be

$$E_{\text{phon}} = N\langle n \rangle h\nu \tag{5}$$

where N is Avogadro's number. The specific heat of the phonon system is

$$C_V^{\text{phon}} = \left(\frac{\partial E_{\text{phon}}}{\partial T}\right)_\nu = Nk_B\left(\frac{h\nu}{k_B T}\right)^2 \frac{e^{h\nu/k_B T}}{(e^{h\nu/k_B T} - 1)^2} \tag{6}$$

Thus, the phonon entropy is

$$S_{\text{phon}} = \int_0^T \frac{C_V^{\text{phon}}}{T}\, dT = R\left[\frac{h\nu/k_B T}{e^{h\nu/k_B T} - 1} - \ln(1 - e^{-h\nu/k_B T})\right] \tag{7}$$

Table 1

Relation between phonon entropy and frequency at $T = 300$ K

$\tilde{\nu} = \nu/c$, where c is the speed of light in a vacuum.

Frequency (ν) (s^{-1})	Wave number ($\tilde{\nu}$) (cm^{-1})	Phonon entropy (S_{phon}) (e.u.)
∞	∞	0
⋮	⋮	⋮
1.2×10^{14}	4000	$\sim10^{-7}$
9.0×10^{13}	3000	$\sim10^{-5}$
6.0×10^{13}	2000	$\sim10^{-3}$
3.0×10^{13}	1000	0.1
2.4×10^{13}	800	0.2
1.2×10^{13}	400	1.0
6.0×10^{12}	200	2.2
3.0×10^{12}	100	3.4
1.5×10^{12}	50	4.8
3.0×10^{11}	10	8.2
3.0×10^{10}	1	12.7
3.0×10^{9}	0.1	17.3
3.0×10^{8}	0.01	21.9
⋮	⋮	⋮
0	0	∞

where R is the gas constant. Table 1 lists the values of the phonon entropy calculated according to eq. 7 at $T = 300$ K for various frequencies. The vibrational wave numbers found in ordinary small molecules are $\tilde{\nu} = 1000$–4000 cm^{-1} and the corresponding phonon entropies are in the range 10^{-1}–10^{-7} e.u., i.e., far too small to make any significant contribution to the free energy. Actually, this can also be understood directly from eq. 4, which can be approximately expressed as

$$\langle n \rangle \simeq \begin{cases} 0 & \text{if } h\nu \gg k_B T \\ k_B T/h\nu & \text{if } h\nu \ll k_B T \end{cases} \tag{8}$$

The above indicates that a high-frequency phonon has much greater energy than $k_B T$, and hence is scarcely excited by thermal motion. This is why the number of high-frequency phonons at room temperature is almost zero, their contribution to the entropy being of course negligible. In contrast, low-frequency phonons are much easier to excite at room temperature, therefore, one cannot ignore their entropy effects.

We now return to the deficit problem in eq. 3. If each of the six vibrational degrees of freedom generated after the binding reaction between insulin and insulin acceptor has a frequency of 10–50 cm^{-1}, then they will contribute an entropy of $\Delta S_{phon} = 49$–29 e.u., which corresponds to a free energy of $\Delta G_{phon} = -T\Delta S_{phon} = -14.7$ to -8.7 kcal/mol. This amount of energy is sufficient for being used to compensate for the unbalanced deficit as occurs in eq. 3.

The above analysis provides us with an interesting clue in that internal motion with very low frequencies ($\tilde{\nu} = 10$–50 cm^{-1}) might exist in biomacromolecules and their complexes. We designate such a region of frequencies the low-frequency region in order to distinguish it from those usually found in ordinary molecules. This kind of internal motion, which exists uniquely in biomacromolecules, must be some kind of collective motion involving many atoms. More important is that, in addition to the explanation of the above thermodynamic deficit, it might possess some significant biological functions as will be discussed later.

1.3. Observed low-frequency motion

Recently, a growing body of evidence [5–9] has indicated that low-frequency internal motion of $\tilde{\nu} = 10\text{–}50\ \text{cm}^{-1}$ clearly exists in biological macromolecules as shown in table 2, which lists the low-frequency modes observed in the Raman spectra for some proteins and DNA. From table 2 we also note the interesting phenomenon that for some proteins, such as insulin and β-lactoglobulin, both monomer and dimer have the same low-frequency peak.

1.4. The existing theoretical models

With low-frequency motions being observed in more and more biological macromolecules, various models have been proposed, attempting to reveal the mechanisms of such interesting internal motions, and they may be classified as follows:

1.4.1. The elastic global model [10]

In this model a protein molecule was likened to a continuous elastic sphere imitating heart 'breathing' or 'pulsation' movement. The following formula in earth dynamics was adopted to calculate the low-frequency wave number of a globular protein:

$$\tilde{\nu} = \frac{1}{2\pi c}\sqrt{\frac{\pi E}{\rho_0 r^2}} \tag{9}$$

where E, ρ_0 and r are the Young's modulus, mass density and radius of the globular protein, respectively. This is a model full of imagination and, at one time, did stimulate other developments in this area, both theoretical and experimental. However, this model does not consider any internal conformation, and hence cannot reflect the sensitivity of the observed low-frequency mode of a protein molecule to a conformational change, as observed by Brown et al. [5]. Besides, contradictory to eq. 9, it was sometimes found (see table 2) that the observed low-frequency wave number for a larger protein molecule was higher than that

Table 2

Observed low-frequency modes in the Raman spectra of biomacromolecules

Biomacromolecules	Molecular mass (Da)	Observed Raman line (cm^{-1})
α-Chymotrypsin [a]	22600	29
Pepsin [a]	35000	32
Lysozyme [b]	14000	25
Insulin [c]	monomer 5800 dimer 11600	22
β-Lactoglobulin [c]	monomer 18000 dimer 36000	25
Concanavalin A [c]	55000	20
Ovalbumin [c]	44000	22
Bovine serum albumin [c]	67000	14
Adolase [c]	158000	32
Thyroglobulin [c]	669000	17
Bovine immunoglobulin G [d]	150000	28 36 (shoulder)
DNA [e]		30

[a] Ref. 5. [b] Ref. 6. [c] Ref. 9. [d] Ref. 7. [e] Ref. 8.

for a smaller one. In particular, it is difficult to explain according to this model why, for insulin and β-lactoglobulin, the monomer and dimer have the same observed low-frequency peak. All these problems actually arise from the fact that the elastic global model treats the entire internal structure of a protein molecule as a 'black box' without considering its conformation.

1.4.2. The normal mode model [11–14]

This model is actually a combination of the classical normal mode theory with modern computer techniques. In principle, it can reach the level of the constituent atoms of a protein molecule, and hence much more detailed information can be obtained. However, in order to realize this degree of detail, the approach is much more computationally demanding. The results thus obtained are very sensitive to the choice or assumption of the potential functions between atoms, which, however, are based on semi-empirical principles. Consequently, for a long time to come, much work can be carried out in following such a line, especially in continuously improving the potentials as well as the computation technique. Moreover, using this model, one usually obtains a frequency spectrum rather than the dominant low-frequency mode, the mode directly corresponding to the observed outstanding low-frequency peak being listed in table 2. Physically speaking, the so-called dominant low-frequency mode is actually that mode whose phonons excited are overwhelming in number and hence whose amplitude is the greatest in the frequency spectrum owing to various favorable factors such as the microenvironment and the distribution of weak bonds [15,16]. In other words, the current normal mode model does not directly present an intuitive physical picture of the dominant low-frequency motion, which, as will be shown later, is a kind of collective internal motion involving a substantial number of atoms in a biomacromolecule and hence is of primary significance in biological functions.

1.4.3. The amorphous model [9]

It is presumed in this model that the vibrations represented by the density of states can be coupled in such a fashion as to produce accordion-like motions [17], breathing motions [18], or any similar kind of collective motion. Therefore, such an interpretation does not rule out the possibility of other explanations and is actually complementary with them. This is an attractive model, especially in helping to gain an understanding of why low-frequency Raman lines of proteins were always broadened.

1.4.4. The quasi-continuity model [17–19]

This model was proposed in an attempt to simplify calculation of the dominant low-frequency motion by identifying the most essential factors and ignoring those that are insignificant. Insofar as the depth of the description is concerned, this model is intermediate between the elastic global and normal mode models, and hence can serve as a means of achieving the best compromise between the two extremes. Unlike the elastic global model, this model can to some extent reflect the internal conformation and microenvironment of a biomacromolecule, however, it treats the constituent atoms as a continuous mass distribution, thus greatly simplifying the calculation in comparison with the discrete normal mode model. An additional merit of the quasi-continuity model is that an intuitive physical picture is correspondingly provided for each of the various types of dominant low-frequency motion in proteins and DNA, which is very useful for investigating biological functions.

In fact, all four of the above models have stimulated developments in this area, albeit at different levels. In addition, it is believed that a successful and complementary combination of those models will certainly benefit studies in this field. However, here we shall focus our discussion on the quasi-continuity model, not only because the formulae derived based on this model are very convenient and successful in calculating the dominant low-frequency modes, but also because the explicit physical pictures described by the quasi-continuity model are quite illuminating and effective in investigating the relevant biological functions even for very complicated biological macromolecules.

2. Methods of calculation

2.1. The origin of low-frequency motion in biomacromolecules

In comparison with ordinary small molecules, a biomacromolecule generally possesses the following two unique features: (1) a series of weak bonds, such as hydrogen bonds and salt bridges, whose distribution and arrangement play a very important role in dictating the higher-order structue of the molecule; (2) a large number of atoms distributed around those weak bonds. Both of these conspicuous features provide an explanation not only for the ease with which a biomacromolecule undergoes conformational change, but also for the occurrence of low-frequency internal motion [20].

The above conception can serve as a criterion in helping one to grasp the essential factors and to ignore the inessential features in order to establish a simple but accurate model for calculating the dominant low-frequency motion. From the above analysis, it is clear that the factors essential to dominant low-frequency internal motion comprise the distribution of mass, the arrangement of weak bonds and the geometry of the internal conformation. Details of how individual atoms fluctuate are not important, since their effects either cancel out each other or reach an internal mutual equilibrium (corresponding to a local energy minimum) in a time much shorter than the period of the low-frequency motion [21]. The most important effect related to the movements of individual atoms is that they might be coupled in such a fashion as to generate a collective low-frequency motion. This kind of collective motion, however, can be deduced directly from the continuity model without needing to consider the detailed behavior of individual atoms. As regards high-frequency vibrations of a molecule, which involve very small relative displacements and very strong chemical bonds, e.g., covalent bonds, between neighboring individual atoms, one must investigate the details of the motions of individual atoms and resort to the discrete model. However, for the low-frequency motion in a biomacromolecule, which involves a relatively much larger effective mass and much weaker force constants (note that the force constant of a hydrogen bond is about two orders of magnitude smaller than that of a covalent bond), and whose mode can be compared with an accordion-like motion, breathing motion, or any kind of collective motion involving many atoms and spanning a much greater distance than the length of a covalent bond, it is not only much more convenient but also physically rational to treat the constituent atoms according to a continuous mass distribution as in the quasi-continuity model. Such a treatment can also be rationalized by drawing a parallel between the quasi-continuity model and Hooke's law. The latter states that, within the elastic limit of any body, the ratio of F, the stress, to x, the strain produced, is constant. As is well known, when a body experiences a strain, all of its constituent atoms must undergo very complicated internal movements. However, it is not necessary for one to follow the scholasticism of worrying about this kind of hair-splitting description. To define uniquely the mechanical state concerned, it suffices for our purposes to use a continuous parameter x as done by Hooke. Therefore, the validity of simplification as carried out in the quasi-continuity model is now readily understood. In fact, the quasi-continuity model and Hooke's law are quite similar as far as the rationality in simplifying the description is concerned. Below, we shall apply the quasi-continuity model to derivation of the equations for calculating the dominant low-frequency motions in α-helix structure, β-structure (including β-sheets and β-barrels) and DNA double-helix structure, the three most fundamental component elements existing in biological macromolecules.

2.2. α-Helix

As is well known, an α-helix has 3.6 residues per turn. An α-helix of n amino acid residues generally has $n-4$ hydrogen bonds, with the i-th one spanning the CO of the i-th residue and the NH of the $(i+4)$-th residue (fig. 1). Therefore, a collective fluctuation of these hydrogen bonds along the axis of the α-helix, coupled with its constituent atoms, will naturally give rise to an accordion-like motion, one of the typical

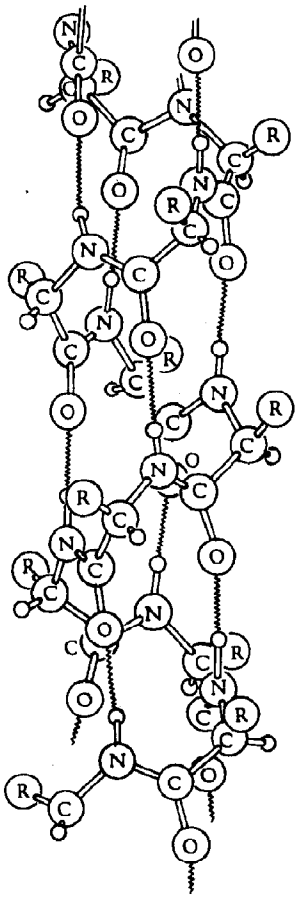

Fig. 1. The α-helix in which the zigzag line denotes the hydrogen bond between the CO of the i-th residue and NH of the $(i+4)$-th residue.

low-frequency modes in biomacromolecules. Based on such a physical picture, an α-helix can be likened to a spring whose mass, however, is not negligible, viz., to a spring with distributed mass (fig. 2). This model characterizes the origin of the low-frequency motion via (1) a series of hydrogen bonds that stabilize the framework of a helical structure, and (2) a continuous mass distribution that further substantiates such a spring-like entity.

However, an α-helix in a protein molecule may be subject to various conditions with respect to its terminal ends, depending on its microenvironment and location. For example, in proteins the following terminal conditions are often found to apply to an α-helix:

(1) One end of the α-helix is linked via a chemical bond to a part of the protein which is very compact and of much greater mass than that of the helix, its other end being attached to a peptide fragment whose environment allows it to move freely together with the accordion-like motion of the α-helix. Under such circumstances, the very compact part of the protein can be treated as a 'hard wall' and the chemical bond as a spring of negligible mass so that the entire system can be simplified to the one illustrated in fig. 3a, where k is the stretching force constant of the α-helix, K the stretching force constant of the chemical bond, and M the mass of the attached peptide fragment.

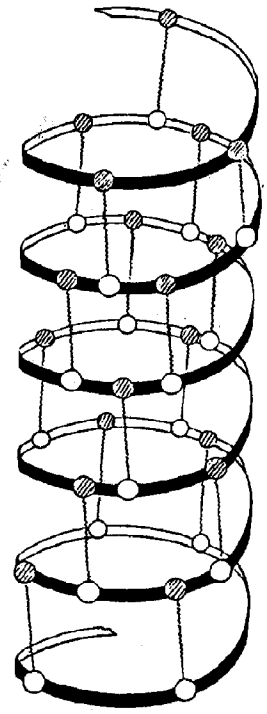

Fig. 2. The α-helix viewed according to the quasi-continuity model. The corresponding hydrogen bonds are represented by the vertical zigzag lines.

Suppose σ is the maximum extent of stretching of the entire spring system, then we have

$$\sigma = \sigma_k + \sigma_K \tag{10}$$

where σ_k and σ_K denote the maximum extents of stretching of the spring k (i.e., the α-helix) and spring K (i.e., the chemical bond between the α-helix and the hard wall), respectively (fig. 3a). According to the condition of force equilibrium

$$k\sigma_k = K\sigma_K \tag{11}$$

as well as eq. 10, we also have

$$\left.\begin{aligned}\sigma_k &= (1-\gamma)\sigma \\ \sigma_K &= \gamma\sigma\end{aligned}\right\} \tag{12}$$

where

$$\gamma = k/(k+K) \tag{13}$$

Suppose the length [22] of the helix axis is L, then when the spring system is in accordion-like motion, the displacement of any point on the helix at any moment can be expressed, without loss of generality, by

$$u(x,t) = (x\sigma_k/L + \sigma_K)\sin \omega t \quad (0 \le x \le L) \tag{14}$$

where ω is the circular frequency. Furthermore, if ρ is the mass per unit length along the axis of the helix,

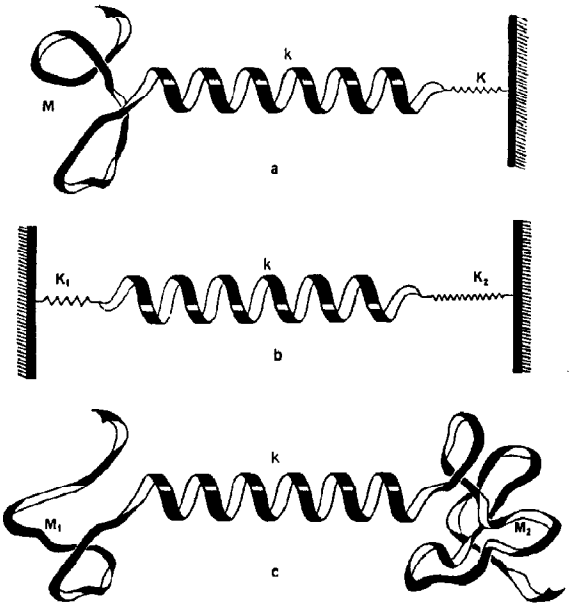

Fig. 3. The three different terminal conditions often found for an α-helix in protein molecules: (a) one end of the α-helix is linked via a chemical bond to a very compact portion of a protein, its other end being attached to a peptide fragment whose environment allows it to move freely together with the accordion-like motion of the helix; (b) both ends of the α-helix are each linked via a chemical bond to a very compact portion of a protein; and (c) the two ends of the α-helix are each attached to a peptide segment that can move freely together with the accordion-like motion of the helix.

then the maximum kinetic energy of a mass element $\rho\Delta x$ of the helix, at a distance x_i from the connective point of the helix with the spring K, is given by

$$\max \Delta T_i = \frac{\rho\Delta x}{2} \max\left(\frac{\mathrm{d}u}{\mathrm{d}t}\right)_{x_i}^2 = \frac{\rho\Delta x}{2}\left[\sigma_K + (x_i\sigma_k)/L\right]^2\omega^2 \tag{15}$$

The total maximum kinetic energy of the spring system will be

$$\max T = \lim_{\Delta x\to 0}\left[\sum_i \max(\Delta T_i)\right] + \frac{M}{2}\max\left(\frac{\mathrm{d}u}{\mathrm{d}t}\right)_{x-L}^2 = \tfrac{1}{2}\omega^2\int_0^L \rho(\sigma_K + x\sigma_k/L)^2\,\mathrm{d}x + M\omega^2\sigma^2/2$$

To a fair approximation, ρ, the mass per unit length of the helix, can be treated as even. Thus, we have

$$\max T = \frac{\rho}{2}\omega^2\int_0^L(\sigma_K + x\sigma_k/L)^2\,\mathrm{d}x + M\omega^2\sigma^2/2 = \tfrac{1}{2}\left\{M + M_{\mathrm{H}}(1+\gamma+\gamma^2)/3\right\}\omega^2\sigma^2 \tag{16}$$

where M_{H} is the mass of the α-helix. On the other hand, the maximum potential of the spring system is

$$\max U = k\sigma_k^2/2 + K\sigma_K^2/2 = K^\dagger\sigma^2/2 \tag{17}$$

where

$$K^\dagger = kK/(k+K) = \gamma K \tag{18}$$

According to energy conservation, i.e., max $T = \max U$, we immediately obtain the wave number of the accordion-like motion:

$$\tilde{\nu} = \frac{\nu}{c} = \frac{\omega}{2\pi c}\sqrt{\frac{K^{\dagger}}{M + (1+\gamma+\gamma^2)M_H/3}} \tag{19}$$

The corresponding thermal amplitude of the α-helix can be determined as follows. According to eq. 4, the average thermal vibrational energy of an oscillator with frequency ν is (note for low-frequency modes we generally have $h\nu \ll k_B T$):

$$\langle \epsilon \rangle_T = \langle n \rangle h\nu = \left.\frac{h\nu}{e^{h\nu/k_B T} - 1}\right|_{h\nu \ll k_B T} \simeq k_B T \tag{20}$$

However, according to eqs. 12, 13 and 17, the maximum potential is

$$\max U = \frac{K^{\dagger}}{2}\left(\frac{\sigma_k}{1-\gamma}\right)^2 = \frac{k}{2(1-\gamma)}\sigma_k^2 \tag{21}$$

Thus, the condition of energy conservation $\langle \epsilon \rangle_T = \max U$ will give

$$\sigma_k = \sqrt{\frac{2(1-\gamma)\langle \epsilon \rangle_T}{k}} = \left.\sqrt{\frac{2(1-\gamma)h\nu/k}{e^{h\nu/k_B T} - 1}}\right|_{h\nu \ll k_B T} \simeq \sqrt{\frac{2(1-\gamma)k_B T}{k}} \tag{22}$$

(2) The two ends of the α-helix are both linked via a chemical bond to a highly compact segment with relatively much larger mass than that of the helix. In this case, the α-helix can be considered as being linked to two hard walls at both ends via two mass-negligible springs whose force constants are K_1 and K_2, respectively, as shown in fig. 3b. For such a spring system in accordion-like motion, the analogous derivation yields

$$\tilde{\nu} = \frac{1}{2\pi c}\sqrt{\frac{k + K^*}{(\alpha_1^3 + \alpha_2^3)M_H/3}} \tag{23}$$

where

$$\alpha_1 = K_2/(K_1 + K_2),\ \alpha_2 = K_1/(K_1 + K_2) \tag{24}$$

$$K^* = K_1 K_2/(K_1 + K_2) \tag{25}$$

and the corresponding thermal amplitude of the α-helix is given by

$$\sigma_k = \sqrt{\frac{2\langle \epsilon \rangle_T}{k + K^*}} \simeq \sqrt{\frac{2k_B T}{k + K^*}} \tag{26}$$

(3) The two ends of the α-helix are both attached to a peptide segment that can move freely together with the accordion-like motion of the helix, so that the whole system can be compared with the one depicted in fig. 3c, where M_1 and M_2 are the respective masses of the two attached peptide segments. The accordion-like motion of this system can also be derived similarly, its wave number being given by

$$\tilde{\nu} = \frac{1}{2\pi c}\sqrt{\frac{k}{M^* + (\beta_1^3 + \beta_2^3)M_H/3}} \tag{27}$$

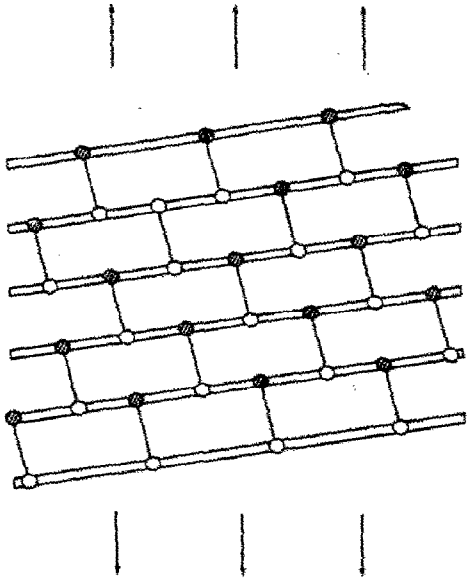

Fig. 4. Illustration obtained by cutting and flattening the flank of the α-helix in fig. 2.

where

$$\beta_1 = M_2/(M_1 + M_2),\ \beta_2 = M_1/(M_1 + M_2) \tag{28}$$

$$M^* = M_1 M_2/(M_1 + M_2) \tag{29}$$

while the corresponding thermal amplitude is expressed by

$$\sigma_k = \sqrt{\frac{2\langle \epsilon \rangle_T}{k}} \simeq \sqrt{\frac{2k_B T}{k}} \tag{30}$$

The problem now remaining concerns the determination of the stretching force constant k for an α-helix, since all other parameters in eqs. 19, 23 and 27 are known or can be easily obtained for any such given system. According to fig. 1 and the relevant analysis in section 2.1, it is clear that the stretching force constant k of an α-helix is essentially related to its constituent hydrogen bonds. In order to determine such a relation, let us first imagine that the flank of the α-helix in fig. 2 is cut off along a straight line parallel to its axis, and then flattened as illustrated in fig. 4. Thus, according to the combination relation of force constants [16], the resultant stretching force constant k for the spring system as shown in fig. 4 can be expressed as

$$k = \frac{1}{\frac{1}{4k_H^a} + \frac{1}{4k_H^a} + \frac{1}{3k_H^a} + \frac{1}{4k_H^a} + \frac{1}{3k_H^a}} \tag{31}$$

where

$$k_H^a = \sqrt{\left(k_H^a \cos\theta\right)^2 + \left(k_H^b \sin\theta\right)^2} = 0.12 \text{ mdyn/Å} \tag{32}$$

where $k_H^s = 0.13$ mdyn/Å and $k_H^b = 0.03$ mdyn/Å [23] are the stretching and bending force constants of the hydrogen bond, respectively, and $\theta \simeq 26°$ is the angle between the helix axis (i.e., the direction of the accordion-like motion) and the individual constituent hydrogen bonds [17]. By using induction, it can be derived that, for an α-helix with n residues, the stretching force constant can be generally expressed as [15]

$$k = \begin{cases} \dfrac{6k_H^\alpha}{5i} & \text{for } j = 0 \\ \dfrac{12k_H^\alpha}{10i + 12/j} & \text{for } 1 \le j \le 4 \\ \dfrac{12k_H^\alpha}{10i + 3 + 12/(j-4)} & \text{for } 5 \le j \le 8 \\ \dfrac{12k_H^\alpha}{10i + 6 + 12/(j-8)} & \text{for } 9 \le j \le 10 \end{cases} \tag{33}$$

where

$$i = \mathrm{INT}\left[\frac{n-4}{11}\right]$$
$$j = (n-4) - 11i \tag{34}$$

where the truncation operator INT represents taking the integral part for the number following it; i.e., INT(9/2) = 4, INT(14/4) = INT(12/4) = 3, INT(2/3) = 0, etc. Note that n in eq. 34 must be greater than 4 according to the definition of an α-helix. In terms of eqs. 32–34, the stretching force constant for any given α-helix can be easily determined.

Let us now take the insulin molecule as an example, through which the calculation model can be fully illustrated. As shown in table 2, the Raman spectra indicate that a dominant low-frequency peak with a wave number of 22 cm^{-1} has been observed for both insulin monomer and dimer. Such a phenomenon cannot be explained in terms of the elastic global model as formulated in eq. 9, according to which it is obvious that the larger the protein molecule is, the smaller the corresponding low-frequency wave number should be. Therefore, it is clear that the observed dominant low-frequency motion must originate from some special internal structure that exists in both insulin monomer and dimer. It is well known that insulin consists of an A chain and a B chain. The A chain contains two helical regions (residues A2–A8 and A13–A20), the B chain containing one rather longer helix (residues B9–B19). Among these helices, only the B9–B19 helix is most likely responsible for the observed low-frequency peak of 22 cm^{-1} [9], since the other two helices (residues A2–A8 and A13–A20) seem to be too short to generate any low-frequency modes around this range [16]. Besides, they are also rather distorted and actually belong to structures of the irregular helix type [24]. Therefore, our attention should first be focused on the B9–B19 helix, which is indicated by the black shading in fig. 5 and is termed the principal helix. Its amino acid sequence is [24]:

Ser-His-Leu-Val-Glu-Ala-Leu-Tyr-Leu-Val- Cys
(B9) (B19)

which consists of 11 amino acid residues, i.e., $n = 11$. Thus, according to eq. 34, we have $i = 0$ and $j = 7$. Substitution of these data as well as eq. 32 into eq. 33 gives

$$k = 12k_H^\alpha/7 = 0.20 \times 10^5 \text{ dyn/cm} \tag{35}$$

On the other hand, we have

$$M_H = \text{total mass of the B9–B19 helix} = 1228 \text{ g/N} \tag{36}$$

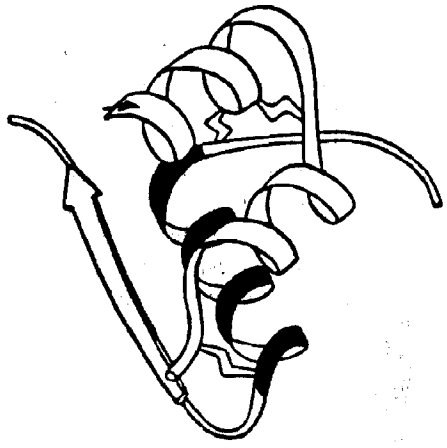

Fig. 5. Schematic drawing of an insulin molecule (with permission from J.S. Richardson), in which the helix (residues B9–B19) is indicated by the black shading.

Residues B1–B8 and B20–B30 that are attached to the two ends of the principal helix are Phe-Val-Asn-Gln-His-Leu-Cys-Gly and Gly-Glu-Arg-Gly-Phe-Phe-Tyr-Thr-Pro-Lys-Ala, respectively [24], having respective values of $M_1 = 901$ g/N and $M_2 = 1346$ g/N. Therefore, according to eqs. 28 and 29, we have $\beta_1 = 0.60$, $\beta_2 = 0.40$ and $M^* = 540$ g/N. Substituting these data as well as eqs. 35 and 36 into eq. 27, we obtain

$$\tilde{\nu} = \frac{1}{2\pi \times 3 \times 10^{10}} \sqrt{\frac{0.20 \times 10^5 \times 6.023 \times 10^{23}}{540 + \left[(0.60)^3 + (0.40)^3\right] \times 1228/3}} = 22.7 \text{ cm}^{-1} \tag{37}$$

which is in excellent agreement with the observed low-frequency Raman peak of 22 cm^{-1} [9]. This is also a

Table 3

A comparison between the observed low-frequency wave numbers for some biological macromolecules and the results calculated in terms of our models

Biological macromolecule	Principal structure involved	Form of motion	Wave number $\tilde{\nu}$ (cm^{-1})	
			Calculated	Observed
α-Chymotrypsin	helix (residues 235–245)	accordion-like motion	29.7 [b]	29 [c]
Pepsin	helix (residues 225–235)		33.0 [b]	32 [c]
Lysozyme	helix 1 (residues 5–15)		27.0 [d]	25 [e]
	helix 2 (residues 25–35)		26.2	
Insulin	helix (residues B9–B19)		22.7 [a]	22 [f]
Immunoglobulin G	β-barrel in V_H domain	breathing motion	28.3 [g]	28 [f]
	β-barrel in C_{HL} domain		28.6 [a]	
	β-barrel in V_L domain		35.8 [a]	36 [f]
Concanavalin A	the β-barrel with 14 strands		19.0 [a]	20 [f]
DNA	various individual intact DNA segments	standing wave	30.3 [a]	30 [h]

[a] Examples given in the present paper. [b] Ref. 15. [c] Ref. 5. [d] Ref. 17. [e] Ref. 6. [f] Ref. 9. [g] Ref. 18. [h] Ref. 8.

very good explanation for the observation of the same maximum low-frequency peak for both insulin monomer and dimer. This is apparently because they both contain the B9–B19 helix, which is the principal structure involved in the accordion-like motion of generating such a dominant low-frequency mode. Furthermore, when $T = 300$ K, substituting eq. 35 into eq. 30, we obtain $\sigma_k = 0.2$ Å, the amplitude of the thermal accordion-like motion of the α-helix.

For an α-helix with a microenvironment different from that above, different equations should be used for calculating $\tilde{\nu}$ (cf. eqs. 19, 23 and 27) and σ_k (cf. eqs. 22, 26 and 30). Nevertheless, the essence of the accordion-like motion originating from the collective fluctuation of the constituent hydrogen bonds is equally valid. In Table 3 are listed more calculated results for the accordion-like motions of the principal α-helices in other proteins, all indicating a good agreement with observations.

2.3. β-Sheet and β-barrel

The model presented above for the accordion-like motion of an α-helix is very successful in elucidating the observed maximum low-frequency peaks for many protein molecules, however, outstanding low-frequency peaks have also been observed for some proteins which contain no α-helical structure but extensive β-structures, the so-called major-β proteins. Therefore, it is necessary to extend the quasi-continuity model to β-structures.

2.3.1. β-sheet

It is well known that in a β-sheet there are a series of hydrogen bonds between its two adjacent strands. The hydrogen bonds are formed between every other backbone CO group of each strand and every other backbone NH group of the adjacent strand (fig. 6), and vice versa [25]. Thus, if an α-helix can be compared to a mass-distributed spring, a β-sheet can of course be compared with a 'rod and spring' mattress as illustrated in fig. 7, where each rod represents a strand, and each spring denotes a hydrogen bond. When carrying out accordion-like motion (fig. 7), such a system will generate the following low-frequency mode * (see the appendix)

$$\tilde{\nu} = \frac{1}{\pi c}\sqrt{[1-\cos(\pi/\mu)]\,\frac{\lambda k_{\mathrm{H}}^{\beta}}{2m}} \tag{38}$$

where μ is the number of the strands of the β-sheet, λ the number of hydrogen bonds between any two neighboring strands, k_{H}^{β} the force constant for each hydrogen bond of such type along the direction of the accordion-like motion, and m the mass of each strand. Moreover, eq. 38 can be approximately extended for calculation of the dominant low-frequency mode of a nonregular β-sheet if the nonregularity does not incur a large relative variance in $\langle m\rangle$, the average mass of a strand, and in $\langle\lambda\rangle$, the average number of hydrogen bonds between two neighboring strands. Under such a circumstance, eq. 38 can be extended to

$$\tilde{\nu} \simeq \frac{1}{\pi c}\sqrt{[1-\cos(\pi/\mu)]\,\frac{\Lambda_{\mathrm{s}} k_{\mathrm{H}}^{\beta}}{2M_{\mathrm{s}}}} \tag{39}$$

where $\Lambda_{\mathrm{s}} = (\mu-1)\langle\lambda\rangle$ is the total number of hydrogen bonds of a nonregular β-sheet, and $M = \mu\langle m\rangle$ its total mass. In fact, the above approximate conditions hold true quite widely for β-sheet in proteins.

Let us now apply eq. 39 to a typical representative of β-sheets in proteins. The statistical analysis of Sternberg and Thornton [26] indicates that the average number of strands per sheet is 4.7, and that most

* Note that eq. 38 is different from eq. 7 of ref. 18. The result calculated in the latter does not generally represent a stable low-frequency mode, whereas that in the former does, as pointed out by E.C. Wong (personal communication).

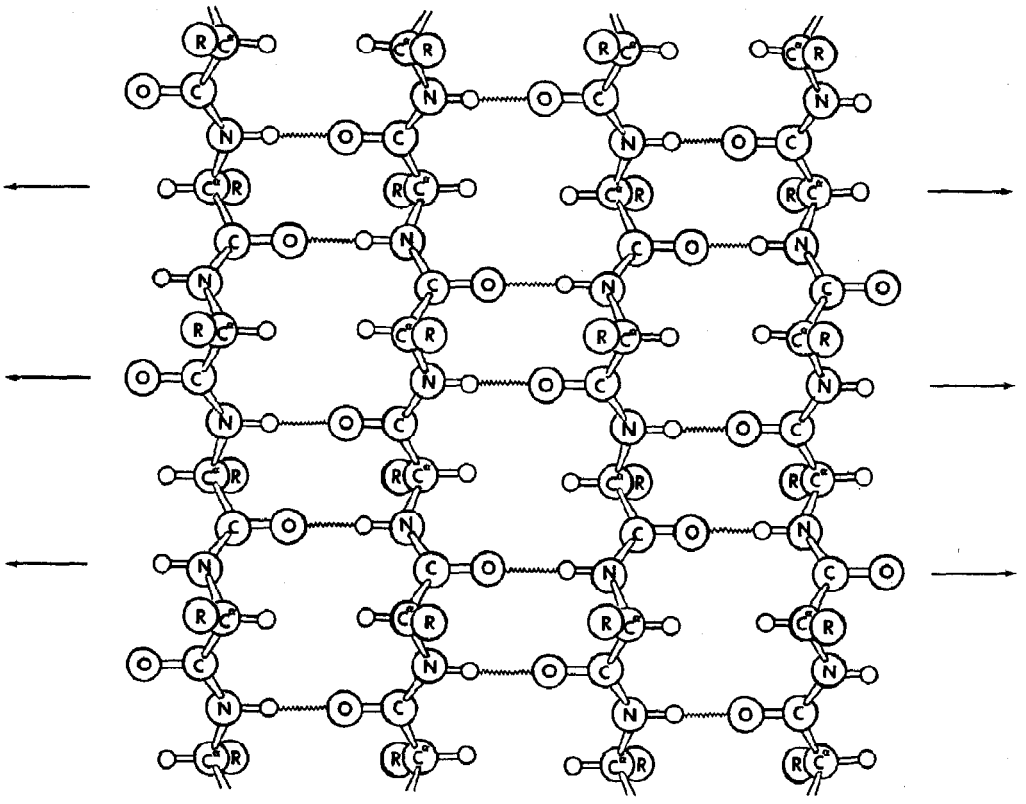

Fig. 6. Antiparallel β-pleated sheet: Hydrogen bonds, shown by zigzag lines, between the NH and CO groups of adjacent strands stabilize the structure. Side chains, represented by R, lie above and below the plane of the sheet.

strands have five to seven residues. Accordingly, as a representative, we can consider a β-sheet with $\mu = 5$ strands, each having six residues plus CH_3CO- and -$NHCH_3$ end groups. The total number of hydrogen bonds [27] for such a β-sheet is $(6+1)\times(5-1)$; i.e., $\Lambda = 28$. However, the hydrogen bonds in an

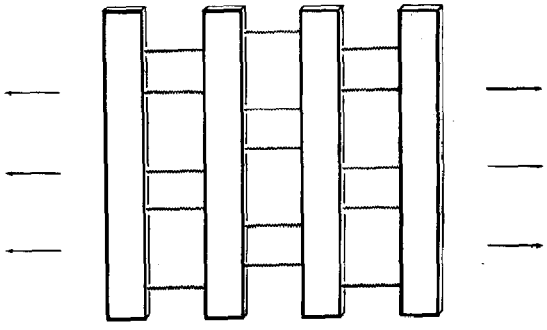

Fig. 7. A 'rods and springs' mattress used to imitate the accordion-like motion of a β-sheet in which there are four strands and five hydrogen bonds between any two adjacent strands.

antiparallel β-sheet are along the direction of its accordion-like motion, while those in a parallel β-sheet are tilted up or down at an angle of $\sim 20°$ [28] from that direction. Therefore, we have

$$k_H^\beta = \begin{cases} k_H^s = 0.13 \times 10^5 \text{ dyn/cm} & \text{for an antiparallel sheet} \\ \sqrt{(k_H^s \cos 20°)^2 + (k_H^b \sin 20°)^2} = 0.12 \times 10^5 \text{ dyn/cm} & \text{for a parallel sheet} \end{cases} \tag{40}$$

where k_H^s and k_H^b have the same definitions as in eq. 32. The mass of each residue in such a representative β-sheet is 111 a.m.u., obtained by taking a weighted average according to the frequencies of various residues in the known β-sheets [29]. Therefore, we have $M_s \simeq 6 \times 5 \times 111 = 3330$ a.m.u. $= 3330$ g/N. Substituting all of these data into eq. 39, we obtain

$$\tilde{\nu} \simeq \frac{1}{\pi \times 3 \times 10^{10}} \sqrt{\left[1 - \cos\left(\frac{\pi}{5}\right)\right] \frac{6.023 \times 10^{23} \times 28}{2 \times 3330} \times k_H^\beta}$$

$$= \begin{cases} 26.6 \text{ cm}^{-1} & \text{for the antiparallel sheet} \\ 25.6 \text{ cm}^{-1} & \text{for the parallel sheet} \end{cases} \tag{41}$$

The above calculation illustrates that a β-sheet with five strands each having six residues can also generate a low-frequency wave number of 26 cm^{-1}. Moreover, the trivial difference between the two values in eq. 41 indicates that the effect due to a tilt angle of $\sim 20°$ in hydrogen bonds is insignificant with respect to the result of a calculated low-frequency mode. Consequently, it is not necessary in subsequent calculations to distinguish k_H^β as belonging to two classes as done in eq. 40. This also justifies the approximate validity of the present model even for a twisted β-sheet [25,30]. Further discussion and a comparison with observations will be given below.

2.3.2. β-Barrel

According to the same conception, low-frequency motion must also exist in a β-barrel (fig. 8). Actually, in this sense, a β-barrel can be compared to a rods and springs cylinder (fig. 9a). When such a cylinder is carrying out a breathing motion (fig. 9b), its frequency can be derived as follows. Assuming ξ is the maximum deviation of each rod from its own equilibrium position during the breathing motion, then the displacement of the i-th rod along the direction as shown in fig. 9b at any time can be described by

$$u_i(t) = \xi \sin \omega t \quad (i = 1, 2, \ldots, 6) \tag{42}$$

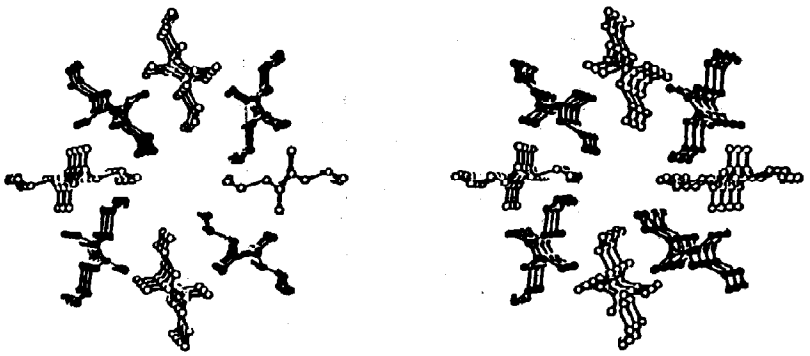

Fig. 8. A stereoscopic drawing depicting a regular β-barrel composed of eight CH_3CO-(L-Val)$_6$-$NHCH_3$ chains, obtained by geometrically fitting the hydrogen bonds between all adjacent chains and as viewed along the axis of the barrel.

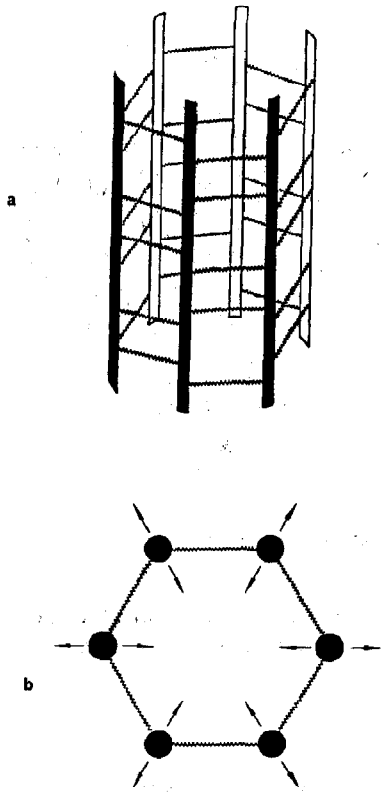

Fig. 9. Schematic representation of (a) a 'rods and springs' cylinder used to imitate the breathing motion of a β-barrel in which there are six strands and five hydrogen bonds between any two adjacent strands, and (b) an illustration of such breathing motion when viewed along the axis of the cylinder.

where ω is the circular frequency of the breathing motion, which, however, will bring about a change in the distance between two adjacent rods, as given by

$$\Delta_{i(i+1)}(t) = |\overline{u_i(t)u_{i+1}(t)}| - |\overline{u_i(0)u_{i+1}(0)}| = 2\xi \sin(\pi/6) \sin \omega t \tag{43}$$

$(i = 1, 2, \ldots, 6;\ i+1 = 1 \text{ when } i = 6)$

where $|\overline{u_i u_{i+1}}|$ represents the distance between the *i-th* and $(i+1)$-th rods. Thus, the total maximum kinetic energy of the system carrying out such a breathing motion is

$$\max T = \frac{m}{2} \sum_{i=1}^{6} \max\left[\frac{\mathrm{d}u_i(t)}{\mathrm{d}t}\right]^2 = 3m\omega^2\xi^2 \tag{44}$$

while the total maximum potential energy is

$$\max U = \frac{5k_{\mathrm{H}}^{\beta}}{2} \sum_{i=1}^{6} \max\left[\Delta_{i(i+1)}(t)\right]^2 = 60k_{\mathrm{H}}^{\beta}\left(\sin\frac{\pi}{6}\right)^2\xi^2 \tag{45}$$

According to energy conservation, i.e., max U = max T, it follows that

$$\tilde{\nu} = \frac{\omega}{2\pi c} = \frac{1}{\pi c}\left(\sin\frac{\pi}{6}\right)\sqrt{\frac{5k_{\mathrm{H}}^{\beta}}{m}} \tag{46}$$

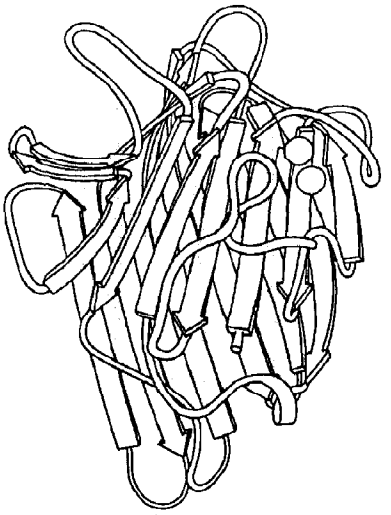

Fig. 10. Schematic drawing of concanavalin A (with permission from J.S. Richardson).

The above derivation can be easily extended to a general case; i.e., for a β-barrel in which there are μ strands and λ hydrogen bonds between any two adjacent strands, we generally have

$$\tilde{\nu} = \frac{1}{\pi c}\left(\sin\frac{\pi}{\mu}\right)\sqrt{\frac{\lambda k_{\mathrm{H}}^{\beta}}{m}} \tag{47}$$

Likewise, under the same conditions as in the case of β-sheets, eq. 47 can be approximately extended to deal with a nonregular β-barrel, as given by the following equation

$$\tilde{\nu} \simeq \frac{1}{\pi c}\left(\sin\frac{\pi}{\mu}\right)\sqrt{\frac{\Lambda_{\mathrm{B}} k_{\mathrm{H}}^{\beta}}{M_{\mathrm{B}}}} \tag{48}$$

where Λ_{B} is the total number of hydrogen bonds in the β-barrel, and M_{B} its total mass.

Let us now take concanavalin A as an example. This molecule has been widely used as a molecular probe in studying cell membrane dynamics and cell division. A conspicuous feature of the molecule is that it contains a large β-barrel with 14 strands [31] but no α-helix at all, as shown by the schematic drawing in fig. 10. For such a β-barrel, we have $\mu = 14$, $M_{\mathrm{B}} \simeq 13\,320$ g/N [32], and $\Lambda_{\mathrm{B}} = 110$ [33]. Substituting these values as well as $k_{\mathrm{H}}^{\beta} \simeq k_{\mathrm{H}}^{s} = 0.13 \times 10^{5}$ dyn/cm [23] into eq. 48, we obtain

$$\nu \simeq \frac{1}{\pi \times 3 \times 10^{10}}\left(\sin\frac{\pi}{14}\right)\sqrt{\frac{110 \times 0.13 \times 10^{5} \times 6.023 \times 10^{23}}{13\,320}} = 19.0\ \mathrm{cm}^{-1} \tag{49}$$

which is quite close to 20 cm^{-1}, the maximum low-frequency peak observed by Painter et al. [9] for concanavalin A. Therefore it is very likely that the dominant low-frequency motion observed in concanavalin A originates from the breathing motion of the β-barrel therein. The calculated results for β-barrels in some other proteins and the corresponding observed values are listed in table 3.

2.4. DNA double-helix structure

If low-frequency internal motion exists in protein molecules, then this kind of motion must also take place in a DNA molecule. This is because a DNA molecule also possesses the following two features

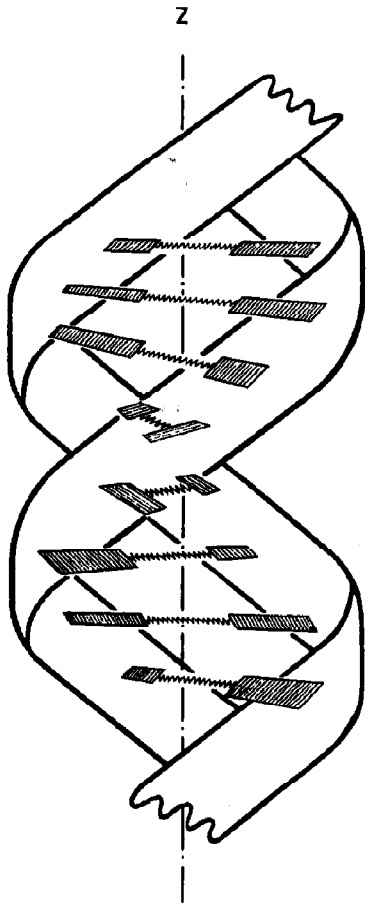

Fig. 11. A 'ribbons and springs' double twiner system used to imitate the collective fluctuations of the complementary hydrogen bonds in a DNA molecule, whose two polynucleotide chains are compared with two right-handed helical ribbons intertwining around the Z-axis, and whose hydrogen bonds between a pair of complementary bases (denoted by hatched rectangles) are compared with a spring, holding the double ribbons together and consecutively rotating around the Z-axis by about 36°.

deemed as prerequisites for the generation of low-frequency internal motion by a molecule: (1) a series of weak bonds such as the complementary hydrogen bonds between its two polynucleotide chains, and (2) a substantial number of atoms distributed around these weak bonds. Let us now consider the low-frequency motion in DNA, the most important genetic molecule in molecular biology.

According to the quasi-continuity model as illustrated earlier for the fundamental structures in proteins, the DNA double helix structure can be likened to a 'ribbons and springs' duplex twiner [19], as shown in fig. 11, where the two DNA polynucleotide chains are schematically expressed by two right-handed helical ribbons intertwining around the same axis Z, while the hydrogen bonds between a pair of complementary bases are expressed by a mass-negligible spring, holding the double ribbons together and consecutively rotating around the Z-axis by about 36°. However, at thermal equilibrium, not all of these base-pairs are closed as held by the intact Watson-Crick hydrogen bonds. Some will be open, corresponding to the rupture of the complementary hydrogen bonds. The closed-open motion is familiarly known as 'breathing',

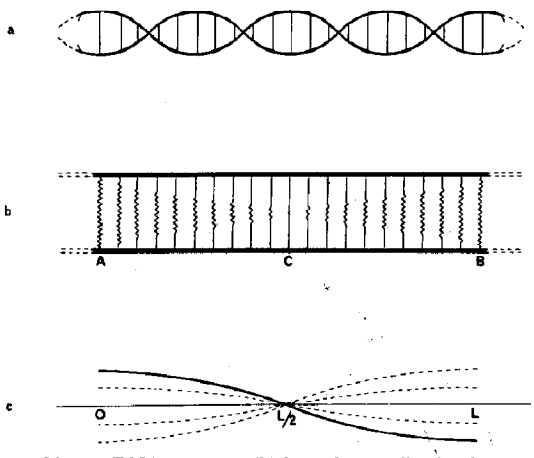

Fig. 12. Illustration to show (a) a piece of intact DNA segment, (b) how the amplitude of a complementary base-pair depends on its location in this segment, and (c) the feature of a standing wave of such a collective motion. In (a), right beyond the two-ends of the segment are the open base-pairs which separate it from the other intact segment along a DNA molecule. In (b), the amplitude at A and B is the greatest, since they are, respectively, the closest to an open base-pair; and the amplitude at C, the center of the segment, is the smallest. In (c), the node is at $Z = L/2$, corresponding to C of (b), and the antinodes are at $Z = 0$ and L, corresponding to A and B of (b), respectively. The continuous curve represents the picture of the standing wave at a given moment, the broken curves depicting it at other instants.

as governed by the following thermodynamic relation

$$\text{closed base-pair} \overset{K_{\text{open}}}{\rightleftharpoons} \text{open base-pair} \tag{50}$$

with, under the general condition [34],

$$\frac{1}{K_{\text{open}}} = \langle n_{\text{base}} \rangle = 38 \tag{51}$$

which means that, on average, for every 38 closed base-pairs there is an open base-pair. Therefore, along a DNA molecule there are actually many 'blocks', each having a consecutive run of closed base-pairs and these blocks are consecutively demarcated by the open base-pairs. Each of these blocks is called an intact DNA segment, whose length may be expressed in terms of n_{base}, the total number of closed base-pairs therein. Although there are many intact segments in a DNA molecule and their n_{base} values are, generally speaking, different and actually fall within the range 20–50 [35], without loss of generality we can take one of them as a representative and investigate its low-frequency internal motion. Suppose the intact segment considered is that with $n_{\text{base}} = 21$, which means the corresponding double helices are held by 21 springs. Because of the effect of the open base-pairs near its two ends (fig. 12a), the forces that hold the double helices are no longer evenly distributed along the segment but depend on the location: the closer it is to the center of the segment, the stronger the force will be. Consequently, the vibrational amplitude between a pair of bases along the direction of a hydrogen bond will also depend on its location: the nearer the base-pair to the center of the intact segment, the smaller its amplitude will be, and vice versa (fig. 12b). Furthermore, although eq. 50 represents a dynamic equilibrium, the base-pair lifetime ($\sim 10^{-2}$ s) [36] is much longer than the period ($\sim 10^{-12}$ s) of low-frequency vibration observed in DNA. Therefore, within a certain interval of time that is much longer than the period of low-frequency vibration but shorter than the conversion period of closed-open motion, only the combined effect of the low-frequency vibration coupled with a particular closed-open state, but not with the closed-open motion itself, needs to be considered for

the present calculation, at least as a first-order approximation. In addition, for an intact segment with $n_{base} = 21 \gg 1$, the amplitude at its center (corresponding to point C in fig. 12b) must be much smaller than those at its two ends (corresponding to points A and B in fig. 12b), and can be virtually neglected. Obviously, this kind of collective motion possesses the features of a standing wave, as shown in fig. 12c, where $Z = L/2$ (corresponding to C in fig. 12b) is the node, and the antinodes are at $Z = 0$ and L (corresponding to A and B in fig. 12b, respectively). The continuous curve represents the picture of the standing wave at a given instant, the broken lines illustrating it at other instants. The vibrational displacement for such a standing wave can be formulated as:

$$u(z,t) = \zeta \cos(\pi z/L) \sin \omega t \tag{52}$$

where Z is the axis of the intact DNA segment, L its length which is actually the distance between two antinodes of the standing wave, ω the circular frequency and ζ the maximum amplitude. Recalling that the number of base-pairs in this segment is n_{base}, the spring that holds the i-th base-pair can be assigned on the Z-axis as:

$$z_i = (i-1)L/(n_{base}-1)$$
$$(i = 1, 2, \ldots, n_{base}) \tag{53}$$

Let the force constant of each such spring be k_{base}, the maximum vibrational potential is thus:

$$\max U = \frac{k_{base}}{2} \sum_{i=1}^{n_{base}} \left[\zeta \cos\left(\frac{\pi z_i}{L}\right)\right]^2 = \frac{k_{base}\zeta^2}{2} \sum_{i=1}^{n_{base}} \cos^2\left(\frac{(i-1)\pi}{n_{base-1}}\right) = (n_{base}+1)k_{base}\zeta^2/4 \tag{54}$$

On the other hand, the maximum kinetic energy of the standing wave in this segment is:

$$\max T = \sum(\rho \Delta z/2) \max\left(\frac{du}{dt}\right)^2 = \int_0^L (\rho\zeta^2\omega^2/2) \cos^2(\pi z/L)\, dz = \rho L\zeta^2\omega^2/4 \tag{55}$$

where ρ is the mass per unit length of the DNA segment along the Z-axis. According to energy conservation, for each of such intact segments in a DNA molecule, we have $\max T = \max U$ (note that the potential energy corresponding to each open base-pair portion is assumed to be zero and its kinetic energy is relatively much smaller when $\langle n_{base} \rangle \gg 1$ and hence can be neglected); it follows that:

$$\tilde{\nu} = \frac{1}{2\pi c}\sqrt{\frac{(n_{base}+1)k_{base}}{\rho L}} = \frac{1}{2\pi c}\sqrt{\frac{(n_{base}+1)k_{base}}{n_{base}\langle m \rangle}} \tag{56}$$

where

$$\langle m \rangle = \frac{\text{total mass of the intact DNA segment}}{n_{base}} = \frac{\text{total mass of the DNA molecule}}{\text{total number of its base-pairs}} \tag{57}$$

We shall now use eq. 56 to calculate the low-frequency modes in DNA molecules. It is well known that a novel feature of the complementary hydrogen bonds in a DNA molecule is that base A (adenine) is always bound to base T (thymine) via two hydrogen bonds, and that base G (guanine) is always bound to base C (cytosine) through three hydrogen bonds, as expressed by A:::T and G⋮⋮⋮C, respectively. Owing to these constraints, a homo-DNA double-helix structure must be either poly(A:::T) or poly(G⋮⋮⋮C). Therefore, we have [23]

$$k_{base} = \begin{cases} 2k_H^s = 0.26 \times 10^5 \text{ dyn/cm} & \text{for poly(A:::T) DNA} \\ 3k_H^s = 0.39 \times 10^5 \text{ dyn/cm} & \text{for poly(G⋮⋮⋮C) DNA} \end{cases} \tag{58}$$

and

$$\langle m \rangle = \begin{cases} 615 \text{ g/N} & \text{for poly(A:::T) DNA} \\ 616 \text{ g/N} & \text{for poly(G:::C) DNA} \end{cases} \tag{59}$$

Substituting eqs. 58 and 59 as well as $n_{\text{base}} = \langle n_{\text{base}} \rangle = 38$ [34] into eq. 56, we obtain

$$\tilde{\nu} = \begin{cases} 27.1 \text{ cm}^{-1} & \text{for poly(A:::T) DNA} \\ 33.2 \text{ cm}^{-1} & \text{for poly(G:::C) DNA} \end{cases} \tag{60}$$

However, for a general DNA molecule, the ratio of (A + T) to (G + C) falls within the range of 1 ± 0.5 [38]. Accordingly, for an intact segment in a general DNA molecule, we should instead use the following approximate data:

$$\left.\begin{aligned} k_{\text{base}} &= 2.5 k_{\text{H}}^{\text{s}} = 0.325 \times 10^5 \text{ dyn/cm} \\ \langle m \rangle &= 615.5 \text{ g/N}, \; n_{\text{base}} = 38 \end{aligned}\right\} \tag{61}$$

Substitution of eq. 61 into eq. 56 yields

$$\tilde{\nu} = \frac{1}{2\pi \times 3 \times 10^{10}} \sqrt{\frac{(38+1) \times 0.325 \times 10^5 \times 6.023 \times 10^{23}}{38 \times 615.5}} = 30.3 \text{ cm}^{-1} \tag{62}$$

which is in very good agreement with the maximum low-frequency Raman peak of 30 cm^{-1} as observed for DNA molecules [8]. It should be noted that an exceptional feature of eq. 56 is that the factor n_{base} appears in both the numerator and denominator, although in the former it assumes the form of $(n_{\text{base}} + 1)$. Simple calculations indicate that the relative change of $\tilde{\nu}$ for different values of n_{base} will always be less than 5% if $n_{\text{base}} \geq 10$. Such a condition can always be valid because the values measured for n_{base} are generally between 20 and 50 [35], with an average value of $\langle n_{\text{base}} \rangle = 38$ [34]. If n_{base} is taken between 20 and 50, the wave number calculated in terms of eq. 56 will fall within the range of 30.6 and 30.2 cm^{-1}, both of which are very close to the observed low-frequency peak of 30 cm^{-1} [8]. This is a very good interpretation of why the observed low-frequency peak for DNA is so sharp and stable at 30 cm^{-1} despite the fact that the values of n_{base} vary appreciably for different intact segments, the individual units generating the standing wave, in a DNA molecule, and that the value of n_{base} is subject to change with time as a consequence of the so-called close-open breathing motion. In other words, almost all the intact segments in a DNA molecule will generate about the same low-frequency wave number. This point should be borne in mind, since it also has a particular significance in biological function as will be discussed later.

3. Biological functions

Our interest in low-frequency internal motion is more concerned with its biological functions. We shall now investigate whether this kind of interesting internal motion plays a role in understanding the following important phenomena in molecular biology.

3.1. What is the dynamic mechanism of the cooperativity in hemoglobin?

A basic and intriguing subject in current molecular biology is the elucidation of the allosterism of oligomeric proteins from a dynamic point of view.

Usually the cooperative effects in an oligoprotein are roughly attributed to the interaction between its subunits. However, through what kind of dynamic channel do the subunits interact with each other,

especially if the binding sites in different subunits are separated by a large distance? Is there any intrinsical relation between the dynamic process and the internal structures of the subunits? If these points are not clear, many cooperative phenomena cannot be interpreted. Let us now take hemoglobin as an example, which consists of two α-subunits and two β-subunits, each having a binding site separated by 25–40 Å from the others! According to the general theory of positive cooperativity, a subunit, after binding to a ligand, will exert, via the interaction of subunits, an influence on the active site of the next subunit so as to increase its binding constant with the next ligand. However, for the following positive cooperative reactions

$$\left.\begin{aligned} &\mathrm{Hb} + \mathrm{O_2} \overset{K_1}{\rightleftharpoons} \mathrm{HbO_2} \\ &\mathrm{HbO_2} + \mathrm{O_2} \overset{K_2}{\rightleftharpoons} \mathrm{Hb(O_2)_2} \\ &\mathrm{Hb(O_2)_2} + \mathrm{O_2} \overset{K_3}{\rightleftharpoons} \mathrm{Hb(O_2)_3} \\ &\mathrm{Hb(O_2)_3} + \mathrm{O_2} \overset{K_4}{\rightleftharpoons} \mathrm{Hb(O_2)_4} \end{aligned}\right\} \tag{63}$$

where Hb denotes hemoglobin, O_2 the oxygen molecule and K_i ($i = 1$–4) the equilibrium constants, the experiments indicate that, rather than $K_4 > K_3 > K_2 > K_1$ as expected according to the general theory of positive cooperativity, we have instead

$$K_4 > K_2 > K_3 > K_1 \tag{64}$$

Why is this so? Obviously this cannot be simply attributed to the general favorable interaction between subunits, especially as here K_3 is actually one order of magnitude less than K_2. However, as shown below, such a phenomenon can be elucidated most naturally from the viewpoint of low-frequency collective motion.

Firstly, let us recall a basic natural phenomenon as can be depicted in fig. 13, where four pendulums are suspended from a wire. Two of the pendulums have the same period and hence form a pair, and so do the other two. Thus, on displacing any one pendulum, the second member of its pair will start to swing, but the others remain almost undisturbed. This is a simple example of resonance, from which we see that a vibrating body can cause a second one to move in sympathy if they have the same intrinsic frequency and are somehow coupled with each other. When two oscillators are in resonance, the energy transfer between them takes place via feedback, and therefore has the following two exceptional characteristics: (1) high efficiency, viz., nearly 100% of the energy can be transferred in such a way if there is no damping; and (2) rapidity, meaning that the speed of resonant exchange in energy is much faster in comparison with that of thermal exchange through collisions.

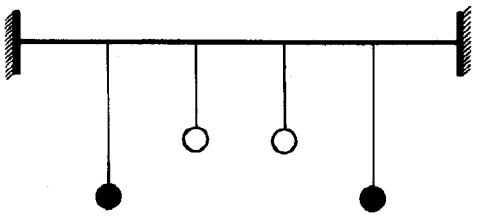

Fig. 13. Two pairs of pendulums suspended from a wire.

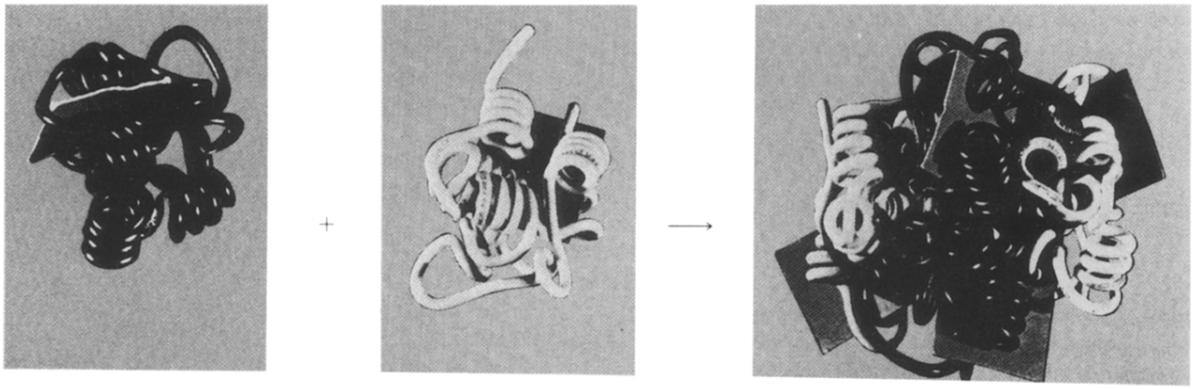

Fig. 14. Illustration demonstrating the formation of hemoglobin from its two α-subunits and two β-subunits. The four subunits are clustered into a tetrahedral orientation, held together by noncovalent interactions (from R.C. Bonhinski [38], with permission from Allyn & Bacon, Inc.).

If we compare the two α-subunits and the two β-subunits of hemoglobin with the two pairs of pendulums in fig. 13, then the energy transfer between two like subunits will be much more efficient than that between two unlike subunits. Moreover, the allosteric transition generally involves substantial intramolecular displacement. However, when a portion of a biomacromolecule is excited to vibrate with a given energy, the low-frequency motions will possess much greater amplitudes and result in much larger displacements of atoms than any high-frequency motions. Therefore, from both energy transfer and internal movement, it can be anticipated that the low-frequency resonance is very likely to play a key role during the allosteric process for hemoglobin.

To make this point more convincing, let us consider fig. 14 where the formation of hemoglobin from its two α-subunits and two β-subunits is illustrated. Three-dimensionally, the four subunits are clustered in a tetrahedral orientation maintained by noncovalent interaction. It is well known that each subunit contains a bound heme group and eight helical segments labeled A–H as shown in fig. 15.

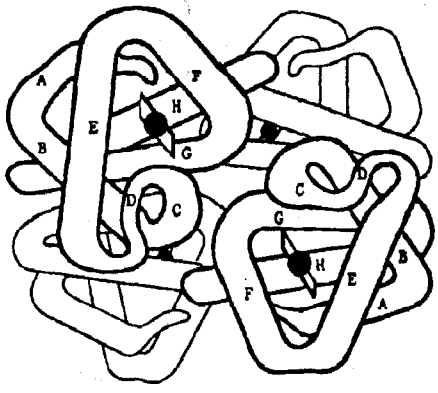

Fig. 15. The hemoglobin molecule: each subunit contains a bound heme group and eight helical segments labeled A–H.

Suppose the eight helices in the α- and β-subunits are denoted by A_α–H_α, and A_β–H_β, respectively. For horse hemoglobin their amino acid sequences are known as [39]:

A_α: Ser-Ala-Ala-Asp-Lys-Thr-Asn- Val-Lys-Ala-Ala-Try-Ser-Lys-Val-Gly
(3) (18)

A_β: Ser-Gly-Glu-Glu-Lys-Ala-Ala- Val-Leu-Ala-Leu-Try-Asp-Lys-Val
(4) (18)

B_α: His-Ala-Gly-Glu- Tyr-Gly-Ala-Glu-Ala-Leu-Glu-Arg-Met-Phe-Leu-Gly
(20) (35)

B_β: Asn-Glu-Glu-Glu- Val-Gly-Gly-Glu-Ala-Leu-Gly-Arg-Leu-Leu-Val-Val
(19) (34)

C_α: Phe-Pro-Thr- Thr-Lys-Thr-Thr
(36) (42)

C_β: Tyr-Pro- Try-Thr-Gln-Arg-Phe
(35) (41)

D_α: His-Phe-Asp- Leu-Ser-His-Gly
(45) (51)

D_β: Asp-Pro-Gly-Ala- Val-Met-Gly
(50) (56)

E_α: Ser-Ala-Gln-Val-Lys-Ala-His-Gly-Lys-Lys- Val-Ala-Asp-Gly-Leu-Thr-Leu-Ala-Val-Gly
(52) (71)

E_β: Asn-Pro-Lys- Val-Lys-Ala-His-Gly-Lys-Lys-Val-Leu-His-Ser-Phe-Gly-Glu-Gly-Val-His
(57) (76)

F_α: Leu-Ser-Asp- Leu-Ser-Asn-Leu-His-Ala
(80) (88)

F_β: Phe-Ala-Ala- Leu-Ser-Glu-Leu-His-Cys
(85) (93)

G_α: Asp-Pro- Val-Asn-Phe-Lys-Leu-Leu-Ser-His-Cys-Leu-Leu-Ser-Thr-Leu-Ala-Val-His
(94) (112)

G_β: Asp-Pro-Glu-Asn-Phe-Arg-Leu-Leu-Gly-Asn- Val-Leu-Ala-Leu-Val-Val-Ala-Arg-His
(99) (117)

H_α: Thr-Pro-Ala- Val-His-Ala-Ser-Leu-Asp-Lys-Phe-Leu-Ser-Ser-Val-Ser-Thr-Val-Leu-Thr-Ser
(118) (138)

H_β: Thr-Pro-Glu-Leu-Gln-Ala-Ser- Tyr-Gln-Lys-Val-Val-Ala-Gly-Val-Ala-Asn-Ala-Leu-Ala-His
(123) (143)

where the numbers in parentheses beneath the residues indicate the sequence orders of the corresponding amino acid residues, counting from the amino end (N-terminal).

From the above description, we see that helices C, D and F contain no more than nine residues. They are too short and unlikely to generate any low-frequency modes of lower than 50 cm^{-1} [15], and hence will not be considered further. The low-frequency accordion-like motions of helices A and H, respectively located near the initial and terminal ends of the polypeptide chain, should be calculated according to the model of fig. 3a and the corresponding expressions, eqs. 13, 18 and 19, while those of helices B, E and G

should be determined according to the model of fig. 3b as well as the corresponding equations (eqs. 23–25). In calculations, however, K_1 and K_2 in eqs. 24 and 25 and K in eqs. 13 and 18 should be substituted by $H(\mathrm{NC'C}^{\alpha}) = 0.19 \times 10^5$ dyn/cm [23], the bending force constant at the folding point, since all helices along the polypeptide chain are folded with each other (figs. 14 and 15). However, the mass M in eq. 19 for the cases of A_α, A_β, H_α and H_β should be substituted by the mass of the corresponding end sequential fragment Val-Leu, Val-Gln-Leu, Lys-Tyr-Arg and Lys-Tyr-His, respectively; therefore, we have

$$\left.\begin{array}{ll} K = 0.19 \times 10^5 \text{ dyn/cm} & \text{for the cases of } A_\alpha,\ A_\beta,\ H_\alpha \text{ and } H_\beta \\ K_1 = K_2 = 0.19 \times 10^5 \text{ dyn/cm} & \text{for the cases of } B_\alpha,\ B_\beta,\ E_\alpha,\ E_\beta,\ G_\alpha \text{ and } G_\beta \end{array}\right\} \tag{65}$$

$$M = \{213, 341, 466, 447\} \text{ g/N} \quad \begin{array}{l}\text{for the cases of} \\ A_\alpha,\ A_\beta,\ H_\alpha \text{ and } H_\beta, \text{ respectively}\end{array} \tag{66}$$

The values of k, the stretching force constant of the helices, can be calculated via eqs. 33 and 34, and were found to be

$$k = \begin{cases} \{6/11, 6/11, 12/25, 12/13, 12/19\}\, k_{\mathrm{H}}^{\alpha} & \text{for } A_\alpha,\ B_\alpha,\ E_\alpha,\ G_\alpha,\ H_\alpha, \text{ respectively} \\ \{6/5, 6/11, 12/25, 12/13, 12/19\}\, k_{\mathrm{H}}^{\alpha} & \text{for } A_\beta,\ B_\beta,\ E_\beta,\ G_\beta,\ H_\beta, \text{ respectively} \end{cases} \tag{67}$$

where k_{H}^{α} is given in eq. 32. Furthermore, according to the amino acid residue sequences of the helices, we have

$$M_{\mathrm{H}} = \begin{cases} \{1616, 1733, 1934, 2091, 2143\} \text{ g/N} & \text{for A, B, E, G, H, respectively} \\ \{1598, 1665, 2157, 2117, 2150\} \text{ g/N} & \text{for A, B, E, G, H, respectively} \end{cases} \tag{68}$$

Using eqs. 13, 18 and 19 as well as the corresponding data in eqs 32 and 65–68 we can calculate $\tilde{\nu}_{A_\alpha}$, $\tilde{\nu}_{H_\alpha}$, $\tilde{\nu}_{A_\beta}$, $\tilde{\nu}_{H_\beta}$, the wave numbers of accordion-like motions carried out by helices A and H in α- and β-subunits, respectively. However, using eqs. 23–25 as well as the corresponding data in eqs. 65 and 67–68, we can calculate $\tilde{\nu}_{B_\alpha}$, $\tilde{\nu}_{E_\alpha}$, $\tilde{\nu}_{G_\alpha}$ and $\tilde{\nu}_{B_\beta}$, $\tilde{\nu}_{E_\beta}$, $\tilde{\nu}_{G_\beta}$, respectively. The results constitute the low-frequency spectra of the α- and β-subunits, as can be expressed by

$$\Gamma_{\alpha_1} = \Gamma_{\alpha_2} = \left\{\tilde{\nu}_{A_\alpha}, \tilde{\nu}_{B_\alpha}, \tilde{\nu}_{E_\alpha}, \tilde{\nu}_{G_\alpha}, \tilde{\nu}_{H_\alpha}\right\} = \{9.4, 43.4, 40.2, 44.7, 7.9\} \text{ cm}^{-1} \tag{69}$$

$$\Gamma_{\beta_1} = \Gamma_{\beta_2} = \left\{\tilde{\nu}_{A_\beta}, \tilde{\nu}_{B_\beta}, \tilde{\nu}_{E_\beta}, \tilde{\nu}_{G_\beta}, \tilde{\nu}_{H_\beta}\right\} = \{10.7, 44.2, 38.0, 44.4, 8.0\} \text{ cm}^{-1} \tag{70}$$

The dynamic data given above will make the elucidation of the aforementioned puzzling phenomena become very natural. According to the general theory of positive cooperativity in oligoproteins, once a subunits has bound to a ligand, the energy released will somehow be transferred to the next subunit, resulting in a conformational change there from a 'tense state' [39] or 'inactivated state' [42,43] to a 'relaxed state' or 'activated state', so as to increase its binding constant with ligand. Now, if this kind of energy is transmitted through a resonance-coupled channel, then the efficiency of energy transfer between two α-subunits or between two β-subunits is much higher than that between an α-subunit and a β-subunit. This is because the low-frequency spectra of the two α-subunits or the two β-subunits are the same (cf. eqs. 69 and 70). In addition, as is well known, the relationship of the resonant amplitude with the difference in frequency is generally described by a particular type of steep function, such as the so-called delta-type function; i.e., a slight difference in intrinsic frequencies between two coupled vibrators will cause the resonance amplitude to diminish remarkably. Therefore, although the differences in the corresponding terms between Γ_α and Γ_β, the low-frequency spectrum of the α-subunit and that of the β-subunit, respectively, fall within the range of only 2.2 cm^{-1}, the efficiency of energy transfer via the resonance-coupled channel between these two subunits will be comparatively significantly weakened. Consequently, the

induced activation process will proceed much more easily between two like subunits than between two unlike subunits. This is the reason for the fact that $K_2 > K_1$ and $K_4 > K_3$ but $K_3 < K_2$, as indicated in eq. 64.

According to such a conception, we can further predict the order in binding ligands by stating that an α-subunit (or β-subunit) is always followed by the other α-subunit (or β-subunit) until both are occupied by ligands, as described by the following sequence

$$[{}^*\alpha_1, \alpha_2, \beta_1, \beta_2] \rightarrow [{}^*\alpha_1, {}^*\alpha_2, \beta_1, \beta_2] \rightarrow [{}^*\alpha_1, {}^*\alpha_2, {}^*\beta_1, \beta_2] \rightarrow [{}^*\alpha_1, {}^*\alpha_2, {}^*\beta_1, {}^*\beta_2] \tag{71}$$

or

$$[\alpha_1, \alpha_2, {}^*\beta_1, \beta_2] \rightarrow [\alpha_1, \alpha_2, {}^*\beta_1, {}^*\beta_2] \rightarrow [{}^*\alpha_1, \alpha_2, {}^*\beta_1, {}^*\beta_2] \rightarrow [{}^*\alpha_1, {}^*\alpha_2, {}^*\beta_1, {}^*\beta_2] \tag{72}$$

where subunits denoted with a superior asterisk to the left represent those having bound a ligand. (Note that the α_1- and α_2-subunits are identical, as are the β_1- and β_2-subunits. Therefore, the sequence order between α_1 and α_2, or between β_1 and β_2, is indistinguishable.) In other words, binding sequences such as

$$\left.\begin{aligned} &[{}^*\alpha_1, \alpha_2, \beta_1, \beta_2] \rightarrow [{}^*\alpha_1, \alpha_2, {}^*\beta_1, \beta_2] \rightarrow \dots \\ &[\alpha_1, \alpha_2, {}^*\beta_1, \beta_2] \rightarrow [{}^*\alpha_1, \alpha_2, {}^*\beta_1, \beta_2] \rightarrow \dots \end{aligned}\right\} \tag{73}$$

are very unlikely to occur. At present, none of the published observations [39–41] violate such a deduction.

Furthermore, let us now consider in greater detail the allosteric transition from the viewpoint of low-frequency collective motion. It is well known that the key to the allosteric transition of hemoglobin lies in the position of the iron atom relative to the porphyrin plane [44]. Since the porphyrin is in contact with about 60 atoms of the globin chain, any change in such a relative position will act as a very effective trigger to initiate a sequence of conformational changes [39]. Observations in detail indicate that after binding a ligand O_2, the iron atom will almost simultaneously move about 0.75 Å into the porphyrin plane [39]. Such a conspicuous internal displacement, which plays a key role in the allosteric transition, is obviously far beyond the reach of any high-frequency amplitudes incurred in a protein through the mere binding of a ligand. We shall now determine what will be expected for the low-frequency amplitude. In terms of eqs. 22 and 26, the low-frequency amplitudes calculated at $T = 300$ K for helices A, B, E, G and H fall within the region of 0.2–0.4 Å. Although these magnitudes are much closer to the value of 0.75 Å in comparison with the corresponding high-frequency amplitudes, they are still much lower than such a critical value. This is rational since, as expected, mere thermal movement certainly cannot trigger the allosteric transition without some additional 'igniting energy'. The igniting energy is none but E^*, the energy released on binding of an oxygen molecule. Since this kind of reaction does not involve covalent binding but merely coordination binding, the energy E^* thus released might be not very large but it is still at least greater than $10k_BT$. If we take this additional igniting energy into account, and replace the thermal energy $\langle\epsilon\rangle_T = k_BT$ in eqs. 22 and 26 by $k_BT + \eta E^*$ where $0 < \eta < 1$, as only a fraction of the binding energy can be used to excite the relevant low-frequency motion, the low-frequency amplitudes thus obtained can certainly reach the critical magnitude of 0.75 Å as required for triggering a successful allosteric transition.

3.2. How can the 'chelate effect' and 'trigger effect' occur in an antibody molecule?

It is well known that antibody molecules generally exhibit two sets of interlinked functions: (a) recognition of foreign cells and macromolecules, and (b) triggering of the events leading to their

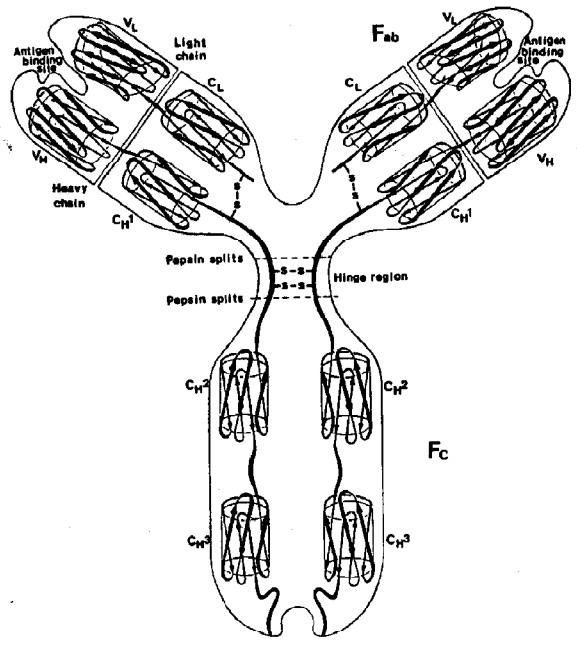

Fig. 16. Schematic representation of an IgG molecule. Divided according to its geometry, the antibody molecule can be considered to consist of two F_{ab} arms and one F_c region. The antigen-binding site is at the terminal of the F_{ab} arm. Divided according to topology, however, the molecule actually consists of two heavy (H) chains and two light (L) chains, which are folded to form 12 domains. These are labelled V_L (variable domain of the light chain), V_H (variable domain of the heavy chain), C_L (constant domain of the light chain) and C_H1, C_H2 and C_H3 (the three constant domains of the heavy chain). Here, 'constant' signifies that a sequence is conserved from one IgG to another, 'variable' denoting sequence variability. Each of the 12 distinct domains contains a β-barrel.

elimination. The former function is taken care of by the two F_{ab} arms of an antibody molecule as reflected by the specific antigen-binding site (fig. 16), while the latter is localized in the F_c region and, under physiological conditions, comes into effect only after antigen binding to both F_{ab} arms [45]. However, the question as to how this 'signal' is transmitted from the F_{ab} to the F_c region remains open to debate. In particular, on going more deeply into the principles of molecular immunology, we are often challenged by asking the following questions: How can antigen binding at one site of an antibody molecule exert an influence upon the other part of the molecule, leading to a remarkable change in conformation of the latter? What is the dynamic process underlying this phenomenon? Through what channel is the energy transported during such an allosteric transition? Here we shall approach these problems from the viewpoint of low-frequency collective motion.

As is known, all antibody molecules are oligomers of a basic four-chain structure, i.e., they consist of two identical 'heavy' (H) and two identical 'light' (L) polypeptide chains, connected at several points by disulfide bridges (fig. 16). The L chain is shorter, comprising about 220 amino acid residues, while the longer H chain has approx. 450 or 475 residues [46–48]. They provide a classic example of a multidomain structure, with 12 independently folded domains making up the whole molecule. The most striking features of the antibody molecule is that each of the 12 distinct domains contains a β-barrel [31,37,49], as depicted schematically in fig. 16. Such an exceptional feature of the conformation not only displays a pleasant harmony in the aesthetic sense, but also gives rise to some special biological functions, as will be seen later. In fig. 16 the domains labelled V_L, V_H and C_L denote the variable domain of the L chain, the variable domain of the H chain and the constant domain of the L chain, respectively. In addition, the three H chain constant domains are designated C_H1, C_H2 and C_H3, respectively. Here, 'constant' signifies that a

Table 4

Physical parameters characterizing the 12 β-barrels of the IgG molecule with respect to the three categories and corresponding low-frequency breathing modes calculated according to eq. 48

Type of β-barrel	Number of β-barrels	Number of strands (μ)	Mass of β-barrel (M_B) (Da)	Number of hydrogen bonds (Λ_B)	Breathing mode ($\tilde{\nu}$) (cm^{-1})
V_H-barrel	2	9 [a]	6640 [a]	50 [a]	28.3
V_L-barrel	2	7 [b]	5440 [a]	42 [a]	35.8
C_{HL}-barrel	8	7 [a]	7104 [a]	35 [a]	28.6

[a] Ref. 49.

[b] Although there are nine strands in the V_L domain, only seven form a β-barrel [49].

particular sequence is conserved from one immunoglobulin to another, with 'variable' meaning that the sequence exhibits variability.

Let us now apply eq. 48 to analysis of the possible low-frequency breathing modes generated respectively by the 12 β-barrels in the IgG antibody molecule. Before proceeding, it should be borne in mind that, within the limits of the accuracy as expressed in eq. 48, the 12 β-barrels can actually be classified into three types as shown in table 4. The β-barrel located in the V_H domain is termed the V_H-barrel and there are two such β-barrels in an antibody molecule. The β-barrel located in the V_L domain is termed the V_L-barrel of which there are also two. All β-barrels located in C_L, C_H1, C_H2 and C_H3 domains, however, belong to the C_{HL}-barrel type. There are in total eight C_{HL}-barrels. The low-frequency modes calculated in terms of eq. 48 for the β-barrels of these three types, as well as the corresponding parameters in the calculation, are listed in table 4. As one can observe, the calculated results are in good agreement with the two maximum low-frequency peaks of 28 and 36 cm^{-1} as observed by Painter and Mosher [7]. Moreover, our calculated results are also a convincing explanation for the fact that the observed low-frequency peak at 28 cm^{-1} is much stronger in intensity than that at 36 cm^{-1}. Obviously, this is because in an IgG antibody molecule there are 10 β-barrels (two in the V_H domains, and eight in the C_L, C_H1, C_H2 and C_H3 domains) that can generate the low-frequency breathing mode of 28 cm^{-1}, however, only two β-barrels (in the V_L domains) can generate the low-frequency breathing mode of 36 cm^{-1}, as indicated in table 4.

We shall now use the above calculated result in the discussion of a number of particular functions carried out by the antibody molecule.

Firstly, let us briefly address the key implications of the dominant low-frequency amplitude, which will help in following the later discussion. As is well known, for a given dominant low-frequency mode, the larger the amplitude is, the more the corresponding phonons will be excited and the greater will be the energy of the relevant domain. Accordingly, the following two aspects are naturally reflected by the amplitude and are both clearly related to biological functions. (a) Conformation: when the dominant low-frequency amplitude of a domain reaches its maximum value, the domain can be considered as more easily reaching (or being triggered to become) the 'relaxed state' [39] or 'activated state' [42]; when the amplitude is at a minimum, however, a favorable conformational change in that domain is unlikely to be triggered, and hence it is quite stable in the 'tense state' [39] or 'inactivated state' [42]. A domain in the former state has a much greater probability of binding to an antigen (or exhibiting the other effector functions) than one in the latter [50]. (b) Energetics: when the dominant low-frequency amplitude of a domain is larger, the energy barrier which must be surmounted for a successful biochemical reaction is more easily overcome. Therefore, the variation of the dominant low-frequency amplitudes of various domains in an antibody molecule will reflect not only the effects of physical coupling but, more importantly, their mutual influence in biological function as well. These two points should be borne in mind while discussing the following effects.

3.2.1. The chelate effect

An antibody performs such a specialized function that once one of the two F_{ab} arms has bound to an antigen, the second arm will also become attached [51], manifesting a remarkable positive cooperativity termed the chelate effect. We would like to understand such a special function from the dynamic point of view. It is well known that the two antigen-binding sites of an antibody molecule are located in the $(V_H + V_L)$ domains of the two F_{ab} arms, respectively (fig. 16). The variable $(V_H + V_L)$ domain is also called the F_V region, reflecting the variations for permitting antibodies to respond to different antigens. It is also well known that the two binding sites, or the two $F_V = (V_H + V_L)$ regions, are coupled with each other through the disulfide bridges (fig. 16). However, according to table 4, both interconnected F_V regions have identical dominant low-frequency spectra [43]; i.e.

$$\Gamma_{F_V^1} = \Gamma_{F_V^2} = \{\tilde{\nu}_{V_H}, \tilde{\nu}_{V_L}\} = \{28.3, 35.8\}\ \mathrm{cm}^{-1} \tag{74}$$

where $\tilde{\nu}_{V_H}$ and $\tilde{\nu}_{V_L}$ denote the low-frequency breathing modes generated by the V_H- and V_L-barrels, respectively. Consequently, the energy can be transferred between the two binding sites through the channel of the following two resonant coupling pairs: the pair of V_H-barrels and of the V_L-barrels (fig. 16). Without loss of generality, let us first consider only the V_H-barrel pair. Supposing that when $t < 0$ there is no coupling relation (constraint), e.g., when the disulfide bridges are broken, the two V_H-barrels are completely independent of each other. Assume, under conditions of random thermal collision, that the breathing motions of two such identical but independent β-barrels are expressed by

$$\left.\begin{aligned} Q_1 &= A\cos\omega_V t \\ Q_2 &= A\sin\omega_V t \end{aligned}\right\}(\text{for } t < 0) \tag{75}$$

where Q denotes the variation of a β-barrel's radius from its equilibrium position due to the low-frequency breathing motion, A is the amplitude and $\omega_V = 2\pi c\tilde{\nu}_{V_H}$ designates the corresponding circular frequency. However, at $t = 0$ there is a coupling relation imposed between them, e.g., the broken disulfide bridges are restored, and the picture of their motions will be very different. Suppose the coupling constant thus introduced between these two β-barrels is x, then the corresponding low-frequency breathing motions will instead be described by [50]:

$$\left.\begin{aligned} Q_1 &= \frac{\sqrt{2}}{2}A\cos\left[\omega_V t + \frac{\pi}{4}\right] + \frac{A}{2}\sqrt{1+\frac{1}{1+2x}}\cos\left[\sqrt{1+2x}\,\omega_V t + \tan^{-1}\left(\frac{-1}{\sqrt{1+2x}}\right)\right] \\ &\simeq \sqrt{2}A\cos\left(\frac{x\omega_V t}{2} - \frac{\pi}{4}\right)\cos\left[\left(1+\frac{x}{2}\right)\omega_V t\right] \\ Q_2 &= \frac{-\sqrt{2}}{2}A\cos\left[\omega_V t + \frac{\pi}{4}\right] + \frac{A}{2}\sqrt{1+\frac{1}{1+2x}}\cos\left[\sqrt{1+2x}\,\omega_V t + \tan^{-1}\left(\frac{-1}{1+2x}\right)\right] \\ &\simeq -\sqrt{2}A\sin\left(\frac{x\omega_V t}{2} - \frac{\pi}{4}\right)\sin\left[\left(1+\frac{x}{2}\right)\omega_V t\right] \end{aligned}\right\}(\text{for } t < 0) \tag{76}$$

A plot for eqs. 75 and 76 is given in fig. 17, from which one can observe: When $t < 0$, i.e., no coupling relation exists between the two β-barrels, the maximum low-frequency displacement attainable by each β-barrel as a result of the breathing motion is A; however, when $t > 0$, i.e., after the coupling relation has been imposed, at a given moment the low-frequency displacement of one V_H-barrel reaches almost as much as $\sqrt{2}A$ and that of the other becomes zero, whereas as the other instant the situation is quite the reverse, clearly exhibiting an alternate variation between these two oscillators. According to the viewpoint of energetics, the above-mentioned physical picture can be described as follows. Due to the resonant coupling effect the energy will be transferred between the two V_H-barrels such that at a given instant one is

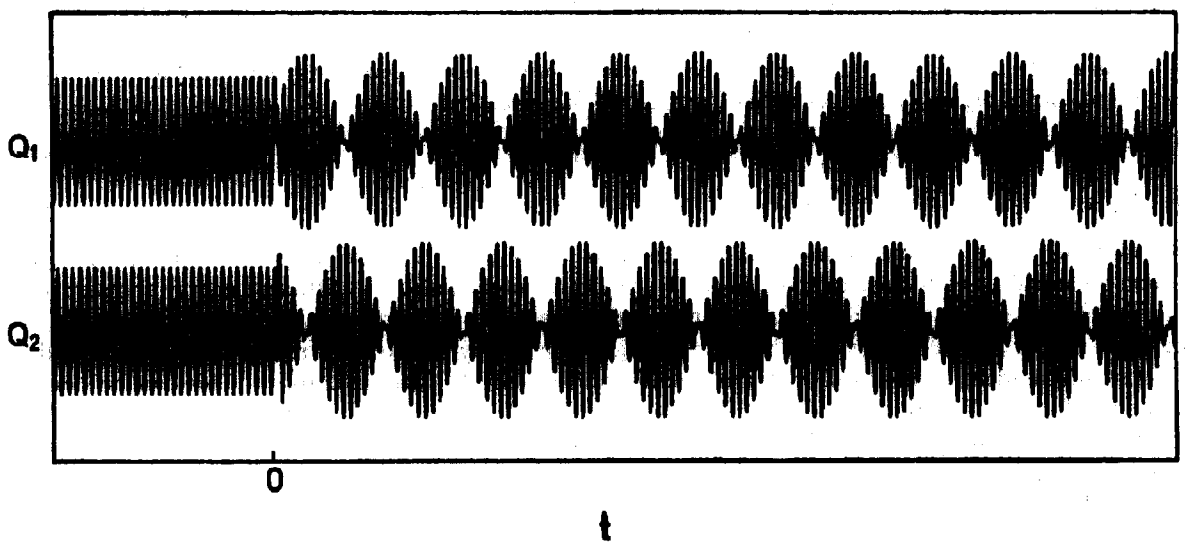

Fig. 17. Plot showing, under conditions of thermal collision, the breathing amplitude of the two β-barrels in an IgG molecule for the case in which no coupling exists between them, i.e., when $t < 0$, and for the case where a coupling relation has been imposed, i.e., when $t > 0$.

capable of possessing an energy amounting to almost double (note that vibrational energy is directly proportional to the square of the amplitude) the maximum energy acquired from thermal collision alone, the energy in the other V_H-barrel decreasing to zero. Nevertheless, once the total energy of the pair has been conferred entirely upon one, the direction of energy transfer will be automatically reversed. If there were no damping effect, such a to-and-fro process of alternate concentration of energy would continue endlessly. Even though there is a damping effect, the basic physical picture of energy transfer via such a resonance-coupled channel would still remain approximately the same except for the intensity as will later on be further discussed.

The above analysis indicates that, because of the coupling resonance, the effect of thermal collision on one binding site can be amplified by almost 100% so as to favor the initial binding of antibody to antigen, since the energy barrier required for such a binding reaction is now comparatively more easily overcome. In particular, on binding of one of the two F_{ab} arms to an antigen, the energy released due to the binding reaction at its $F_V = (V_H + V_L)$ region can be transferred very efficiently to the other F_{ab} arm through the channels of both the V_H- and V_L-barrel resonant coupling pairs. Note that the proportion of this energy is much greater than that of the thermal collision energy, and hence the region of the second F_{ab} arm will be driven into undergoing a dramatic increase in low-frequency displacement. This process actually corresponds to so-called induced activation [42], which markedly increases the binding ability of the second F_{ab} arm to an antigen, as is reflected by the chelate effect occurring in antibody molecules.

3.2.2. The trigger effect

As mentioned above, the effector functions localized in the F_c region of an antibody molecule come into effect only after antigen binding to its F_{ab} arm. Therefore, the two F_{ab} arms can be compared with a pair of antennae (or feelers) of an insect, whose contact with an object promptly yields a signal, resulting in a series of instinctive responses. Actually, the findings of Schlessinger et al. [52] indicate that the binding of antigen to the F_{ab} arm induces an allosteric transition in IgG and that this transition may be a key step in the effector activation process. Let us now use the concept of low-frequency resonance to elucidate how

this kind of signal can be transmitted from the F_{ab} to the F_c region, or the way in which the allosteric transition in the F_c region is triggered by antigen binding to the F_{ab} arm.

From fig. 16 as well as table 4 we can see that the dominant low-frequency spectra [43] for the two F_{ab} arms and the F_c region of an IgG antibody molecule are given by:

$$\Gamma_{F_{ab}^1} = \Gamma_{F_{ab}^2} = \{\tilde{\nu}_{V_H}, \tilde{\nu}_{V_L}, \tilde{\nu}_{C_L}, \tilde{\nu}_{C_H^1}\} = \{28.3, 35.8, 28.6, 28.6\}\ \text{cm}^{-1} \tag{77}$$

$$\Gamma_{F_c} = \{\tilde{\nu}_{C_H^2}, \tilde{\nu}_{C_H^2}, \tilde{\nu}_{C_H^3}, \tilde{\nu}_{C_H^3}\} = \{28.6, 28.6, 28.6, 28.6\}\ \text{cm}^{-1} \tag{78}$$

Comparison of eqs. 77 and 78 indicates that there are three dominant low frequencies in the F_{ab} region which are equal or very close to those in the F_c region. Consequently, very efficient energy transfer must occur between the F_c and F_{ab} regions through the channel of the resonant coupling mechanism. In particular, after both F_{ab} arms have bound to antigen, the energy thus transferred to the F_c region will be further increased in comparison with the binding of only one F_{ab} arm to antigen. This can be demonstrated as follows. Without loss of generality, we shall consider only the C_H3-barrel in the F_c region as an example, investigating the amplitudes of its breathing motion for various cases. First, if there is no resonant coupling effect at all, the breathing motion of the β-barrel results from thermal collision alone, and can be expressed by

$$Q = A \cos \omega_c t \tag{79}$$

where $\omega_c = 2\pi c \tilde{\nu}_{C_H^3}$ is the corresponding circular frequency, A being the amplitude for the case of thermal motion alone. Second, if incorporating the effect of resonant coupling with the binding of one F_{ab} arm to antigen, the breathing motion of the β-barrel is described by [50]

$$Q^* \simeq -A^* \sin\left(\frac{x\omega_c t}{2}\right) \sin[(1 + x/2)\omega_c t] \tag{80}$$

where x is the resonant coupling constant, and A^* the amplitude in the case of thermal motion plus the energy released from binding of an antigen at the F_{ab} arm. Third, when both F_{ab} arms bind to antigen, then instead of eq. 80 we have

$$Q^{**} \simeq \frac{-4}{3} A^* \sin\left(\frac{9x\omega_c t}{16}\right) \sin\left[\left(1 + \tfrac{15}{16}x\right)\omega_c t\right] \tag{81}$$

The plots for eqs. 79–81 are illustrated by fig. 18a–c, respectively. As shown by fig. 18a and b, the energy released by binding of an antigen at the F_{ab} arm is much greater than that of thermal collision and hence drastically increases the amplitude at the F_c region through the channel of resonant coupling. This is why the effector functions at the F_c region come into effect only after the occurrence of antigen binding. Furthermore, due to the effects of both F_{ab} arms, the maximum amplitude in the F_c region (fig. 18c) is 4/3-times that driven by only one F_{ab} arm (fig. 18b). In other words, the maximum energy transferred to the F_c region will be further increased up to $(4/3)^2 \simeq 1.8$-times compared with that in the case of only one F_{ab} arm. From the dynamic point of view, this provides a very good explanation for the finding by Pecht et al. [53] that for complement fixation (one of the antibody effector functions) both F_{ab} arms must bind antigen. This also clarifies why, for a productive effect of 'signal transfer' from the F_{ab} to F_c regions, intact disulfide bonds in the hinge region (fig. 16) of the antibody are required [52,54], since they somehow play a bridging role so that the energy can be transferred between different regions and domains very efficiently through the channel of resonant coupling.

In summary, the dynamic mechanism underlying the allosteric transition in an antibody molecule can be illustrated by the following physical picture. Once one of the F_{ab} arm has bound to an antigen, the energy released due to the binding reaction will, via the channel of resonant coupling, be transferred to the other F_{ab} arm, thus triggering the latter into undergoing a favorable conformational change for antigen

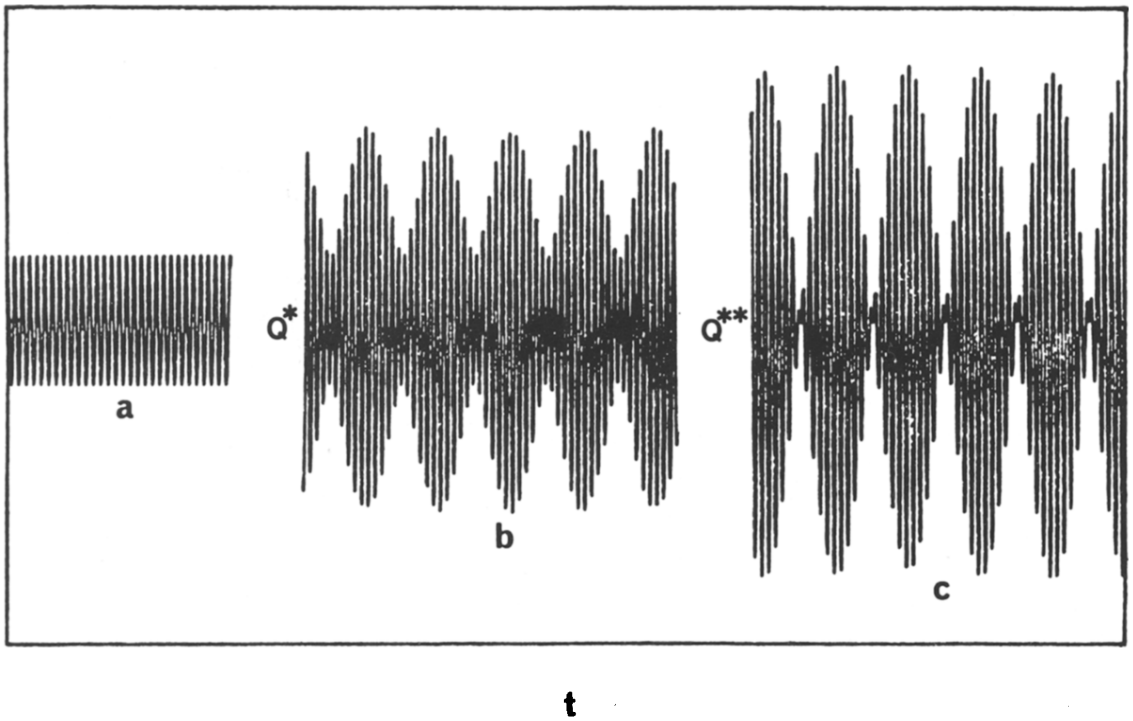

Fig. 18. Plot demonstrating the variation in amplitude of the breathing motion of the β-barrel in the F_c region of an antibody molecule in the cases where the breathing motion is driven by: (a) thermal collisions alone, without resonance coupling occurring; (b) the resonance coupling effect resulting from the energy released through binding of one F_{ab} arm to antigen and (c) resonance coupling effect as a consequence of the energy released via binding of both F_{ab} arms to antigen.

binding. This is the so-called chelate effect. During this process, part of the energy might also be transferred to the F_c region and induce a conformational change there, however, the energy released from antigen binding to only one arm is generally not large enough to overcome the barrier to successful triggering at the F_c region. However, after binding of both F_{ab} arms to antigen, the maximum energy transferred to the F_c region through the resonant coupling mechanism is increased up to almost 180% (fig. 18c), and hence is capable of triggering a drastic, favorable conformational change in the F_c region, which is necessary for the antibody molecule to begin carrying out its effector functions.

Consequently, this kind of allosteric transition is actually 'resonance-controlled', and hence the trigger here can be described as a 'resonance-controlled trigger' in contrast to the concept of a 'diffusion-controlled reaction' in enzyme kinetics [55–57]. By introducing such a concept, one is able, in principle, to calculate the lower time limit [50] for an allosteric transition, one of the most fundamental limiting scales in molecular biology but also one of the most difficult quantities as regards accessibility to observation. Moreover, the dynamic picture illustrated here provides us with a classic example, once again manifesting the beautiful harmony in nature between structure and function.

3.3. How is DNA open enough for intercalation by large drugs?

From the dynamic point of view, how do drugs and dyes intercalate into DNA? Or, how do the 'holes' on DNA become sufficiently open for intercalators to gain entrance into (or exit from) DNA? Here, each of the so-called holes is surrounded structurally by two nearest-neighbor base-pairs of a DNA molecule and their complementary hydrogen bonds as well as the corresponding polynucleotide chains (fig. 11). As

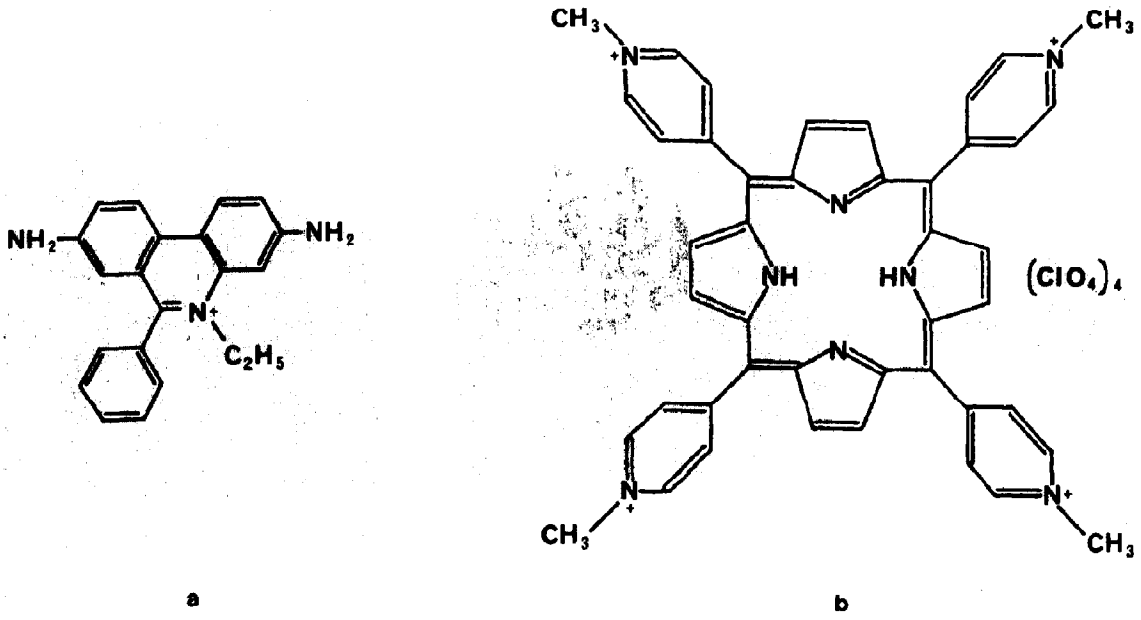

Fig. 19. Structure of the intercalators (a) ethidium and (b) *meso*-tetra(4-*N*-methylpyridyl)porphin tetraperchlorate.

is known, these holes are generally of about equal size to small intercalators, e.g., ethidium (fig. 19a), but certainly much smaller than larger ones, such as *meso*-tetra(4-*N*-methylpyridyl)porphin tetraperchlorate (fig. 19b) (henceforth referred to as porphin). However, the elaborate calculations carried out by Zhou et al. [58] indicate that, if the hole, or 'sink' [56], is of the same size as the intercalator, the probability of a successful intercalation will be extremely low, far lower than the results of observations [59]. Needless to say, the larger intercalators seem simply to be unable to penetrate the hole in order for successful intercalation to result. Nevertheless, according to the experimental results of Fiel and Munson [60], even the porphin, despite its great bulk (fig. 19b), is still capable of intercalating into DNA. This appears to be a perplexing problem. Below, we shall attempt to gain an understanding of such a phenomenon from the viewpoint of the low-frequency collective motion in DNA.

According to section 2.4, each of the intact segments in a DNA molecule can generate a low-frequency standing wave, whose wave number can be calculated from eq. 56. It is also known from the foregoing that the low-frequency standing waves generated by different intact segments of a DNA molecule have approximately the same wave number of $\sim 30\ \mathrm{cm}^{-1}$, which is well in agreement with observations [8]. In other words, the various intact segments in a DNA molecule possess about the same intrinsic low frequency. However, the intact segments are not isolated, but coupled together [61,62] along the DNA molecule through the short open base-pair segments as illustrated in fig. 20a and b for linear and circular DNA, respectively. In fact, from the viewpoint of resonance coupling, all DNA molecules whose two ends are separated can be classified as a linear-type coupling system, all those in which both ends are linked being ascribed to the circular type [61], as depicted schematically in fig. 21a and b, respectively.

Taking the coupling effect into account, the displacement of the i-th oscillator is generally expressed by [62]:

$$Q_i = \sum_{l=1}^{n_p} c_i^l A_l \cos(\omega_l t + \phi_l), \qquad (82)$$

$$(i = 1, 2, \ldots, n_p)$$

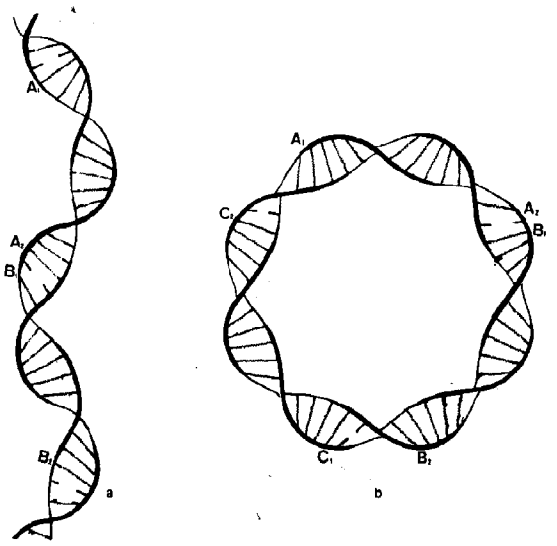

Fig. 20. Illustration depicting the features of the intact segments and their couplings through the short open segments in a DNA molecule: (a) linear coupling, (b) circular coupling. Each spring represents a set of intact hydrogen bonds between a closed base-pair, the broken lines denoting the lack of hydrogen bonds in the open base-pairs. For example, A_1A_2 and B_1B_2 in (a) are two intact segments, which are coupled together through the short open segment A_2B_1, etc. For simplicity, the number of base-pairs drawn here in an intact segment is much smaller than that in a real DNA molecule.

where n_p is the number of coupled oscillators, ω_l and c_i^l being given as follows [62]:
(1) For linear coupling

$$\omega_l = \omega\sqrt{1 - 2\lambda\cos\left(\frac{l\pi}{n_p + 1}\right)}, \tag{83}$$

$$\begin{cases} c_1^l = 1 \\ c_2^l = 2\cos\left(\dfrac{l\pi}{n+1}\right) \\ c_j^l = c_2^l c_{j-1}^l - c_{j-2}^l, \ (j = 3, \ldots, n_p) \end{cases} \tag{84}$$

(2) For circular coupling

$$\omega_l = \omega_0\sqrt{1 - 2\lambda\cos\left(\frac{2l\pi}{n}\right)}, \ (n_p \geq 3) \tag{85}$$

$$c_j^l = \begin{cases} \cos\left[\dfrac{2(j-1)l\pi}{n_p}\right], & \text{for } l = 1, 2, \ldots, \left[\dfrac{n_p}{2}\right] \\ -\sin\left[\dfrac{2(j-1)l\pi}{n}\right], & \text{for } l = \left[\dfrac{n_p + 2}{2}\right], \ldots, n_p - 1 \\ 1, & \text{for } l = n_p \end{cases} \tag{86}$$

where ω is the intrinsic frequency of each individual oscillator, λ the coupling constant [62], and $[X] = \mathrm{INT}[X]$ represents the integral part of X. The coefficients A_l and phases ϕ_l in eq. 82 are determined according to the initial conditions, which can be formulated as follows. Suppose that, when $t \leq 0$, coupling

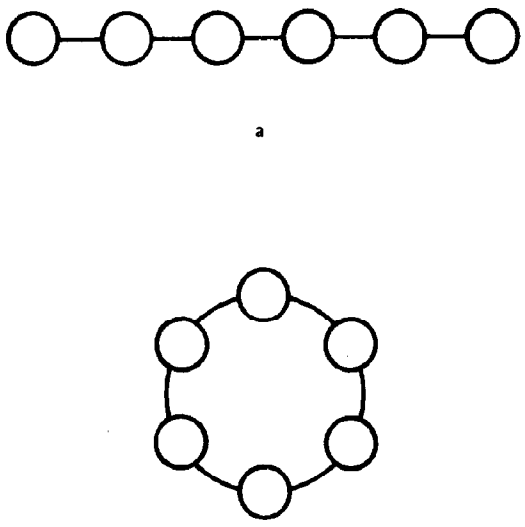

a

Fig. 21. Schematic drawing of (a) linear coupling and (b) cyclic coupling. Each circle represents an oscillator, with the existence of coupling between two oscillators reflected by a solid line.

among the n_p intact segments is absent, i.e., the individual intact segments are completely independent of each other, carrying out low-frequency motion only under conditions of random thermal collisions with solvent molecules. Then, the low-frequency displacements for the n_p oscillators can be generally described by the following equations:

$$Q_i = A\cos(\omega t + \phi_i^0), \text{ for } t \leq 0 \quad (i = 1, 2, \ldots, n_p), \tag{87}$$

where A is the maximum low-frequency amplitude that an oscillator can attain when driven by random thermal collision, ω is approximately equal to 5.65×10^{12} s^{-1} (corresponding to a wave number of $\tilde{\nu} = 30$ cm^{-1} as observed for DNA [8]), and ϕ_i^0 reflects the phase difference among the n_p independent oscillators. Now suppose that coupling is imposed for $t > 0$, i.e., the intact segments are linked to each other through the short open base-pair segments to form a linear or circular DNA molecule. Due to inter-segment coupling effects, the corresponding low-frequency motions will no longer be described by eq. 87, but by eq. 82, in which ω_l and c_i^l are given by eqs. 83 and 84 or eqs. 85 and 86 for linear or circular coupling, respectively, with A_l and ϕ_l being determined by the initial conditions for the system concerned. When $t = 0$, according to eq. 87, we have

$$\left.\begin{aligned} Q_i &= A\cos\phi_i^0 \\ \dot{Q}_i &= -A\omega_0 \sin\phi_i^0 \end{aligned}\right\} \text{ when } t = 0 \quad (i = 1, 2, \ldots, n_p). \tag{88}$$

signifying that the initial conditions are actually reflected by ϕ_i^0, the values of the initial phases.

As an example, we shall discuss the case of cyclically coupled DNA with eight intact segments. According to eqs. 85 and 86, we have

$$\left.\begin{aligned} &\omega_1 = \omega_7 = \omega\sqrt{1 - \lambda\sqrt{2}}\,, \\ &\omega_4 = \omega\sqrt{1 + \lambda\sqrt{2}}\,, \end{aligned}\right\} \quad \omega_3 = \omega_5 = \omega\sqrt{1 + \lambda\sqrt{2}} \quad \left.\begin{aligned} &\omega_2 = \omega_6 = \omega \\ &\omega_8 = \omega\sqrt{1 - \lambda\sqrt{2}} \end{aligned}\right\} \tag{89}$$

and

$$C^1=\begin{bmatrix}1\\ \frac{\sqrt{2}}{2}\\ 0\\ -\frac{\sqrt{2}}{2}\\ -1\\ -\frac{\sqrt{2}}{2}\\ 0\\ \frac{\sqrt{2}}{2}\end{bmatrix},\quad C^2=\begin{bmatrix}1\\ 0\\ -1\\ 0\\ 1\\ 0\\ -1\\ 0\end{bmatrix},\quad C^3=\begin{bmatrix}1\\ -\frac{\sqrt{2}}{2}\\ 1\\ \frac{\sqrt{2}}{2}\\ -1\\ \frac{\sqrt{2}}{2}\\ 0\\ -\frac{\sqrt{2}}{2}\end{bmatrix},\quad C^4=\begin{bmatrix}1\\ -1\\ 1\\ -1\\ 1\\ -1\\ 1\\ -1\end{bmatrix},$$

$$C^5=\begin{bmatrix}0\\ \frac{\sqrt{2}}{2}\\ -1\\ \frac{\sqrt{2}}{2}\\ 0\\ -\frac{\sqrt{2}}{2}\\ 1\\ -\frac{\sqrt{2}}{2}\end{bmatrix},\quad C^6=\begin{bmatrix}0\\ 1\\ 0\\ -1\\ 0\\ 1\\ 0\\ -1\end{bmatrix},\quad C^7=\begin{bmatrix}0\\ \frac{\sqrt{2}}{2}\\ 1\\ \frac{\sqrt{2}}{2}\\ 0\\ -\frac{\sqrt{2}}{2}\\ -1\\ -\frac{\sqrt{2}}{2}\end{bmatrix},\quad C^8=\begin{bmatrix}1\\ 1\\ 1\\ 1\\ 1\\ 1\\ 1\\ 1\end{bmatrix}. \tag{90}$$

When DNA molecules are in thermally governed environment, it is more appropriate to use random initial conditions. For the following initial phases generated by a random number generator [63]

$$\left.\begin{matrix}\phi_1^0=57^\circ, & \phi_2^0=317^\circ, & \phi_3^0=352^\circ, & \phi_4^0=46^\circ\\ \phi_5^0=222^\circ, & \phi_6^0=303^\circ, & \phi_7^0=161^\circ, & \phi_8^0=42^\circ\end{matrix}\right\}, \tag{91}$$

we find, in terms of eqs. 82, 85, 86 and 88, that

$$\left.\begin{matrix}\phi_1\approx 49.2^\circ\\ \phi_2\approx 2.4^\circ\\ \phi_3\approx 49.9^\circ\\ \phi_4\approx -8.8^\circ\\ \phi_5\approx -17.4^\circ\\ \phi_6\approx 86.7^\circ\\ \phi_7\approx -9.4^\circ\\ \phi_8\approx 5.2^\circ\end{matrix}\right\}\left\{\begin{matrix}A_1\approx 0.562A\\ A_2\approx -0.598A\\ A_3\approx 0.436A\\ A_4\approx -0.362A\\ A_5\approx -0.482A\\ A_6\approx -0.728A\\ A_7\approx 0.515A\\ A_8\approx 0.321A\end{matrix}\right\}. \tag{92}$$

Substituting eq. 92 as well as eqs. 89 and 90 into eq. 82, we obtain $Q_i(t)$ $(i=1, 2, \ldots, 8)$, which is plotted in fig. 22.

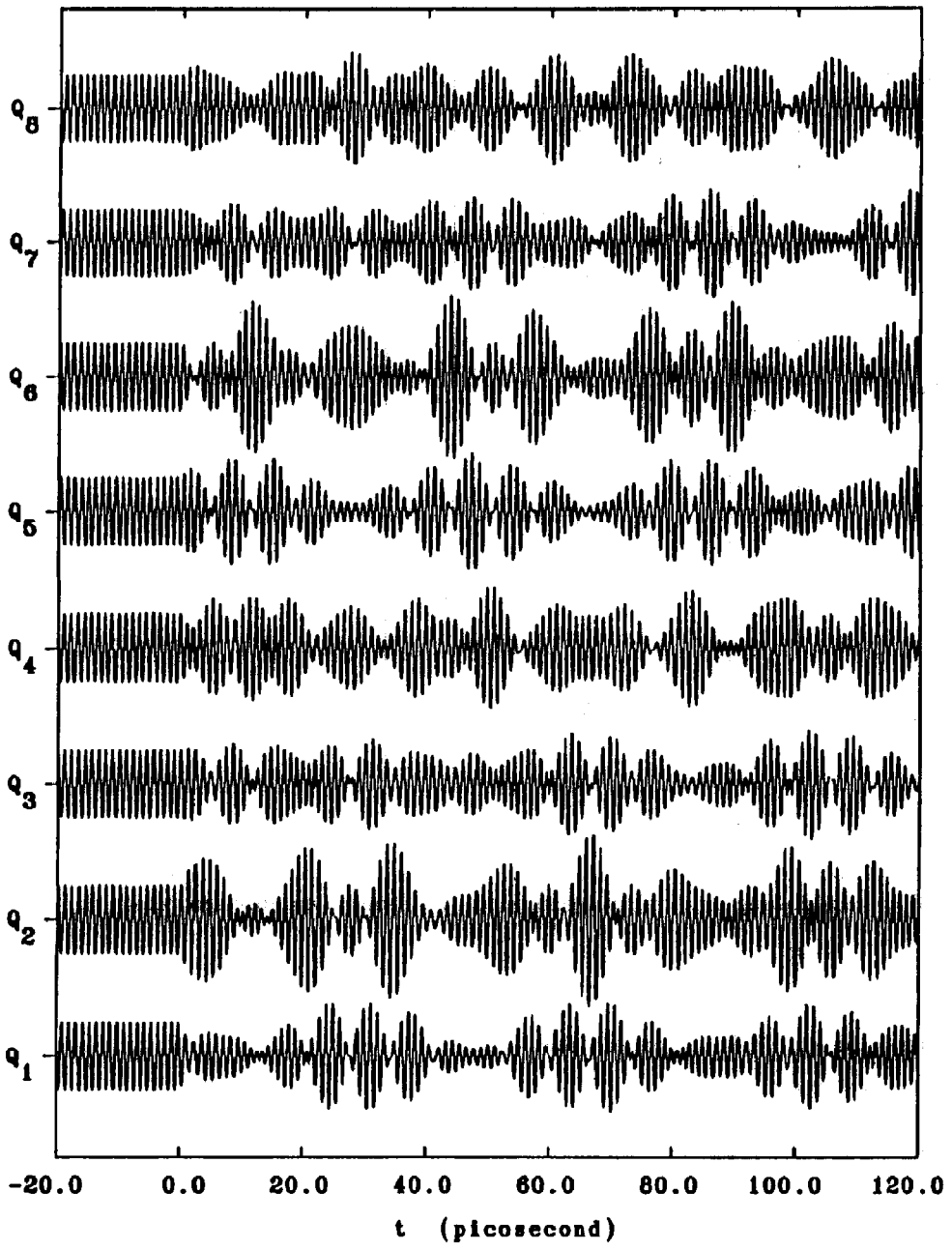

Fig. 22. Plot of low-frequency amplitudes of eight cyclically coupled intact segments under the initial condition of eq. 91 as assigned by a random number generator [63]. Under such a condition, the maximum amplitudes of the second, fourth, sixth and eight intact segments can increase 2.5-fold and the corresponding energies 6.25-fold as compared to the case without coupling effects. Note that the fourth and eighth intact segments require longer periods of time for significant increase in amplitude: this effect is therefore not shown in this figure in which the latest time point is at 120 ps. The plot was derived for a coupling constant of 0.1 and a wave number of 30 cm^{-1} [8] which corresponds to a frequency of 5.65×10^{12} s^{-1}.

As one can observe from fig. 22, when $t \leq 0$, i.e., when no coupling effect is present, the amplitudes of the eight intact segments are equal and remain invariant. This is because they each carry out independent low-frequency motion under conditions of random thermal collisions with solvent molecules. However, when $t > 0$, i.e., with the presence of the coupling effect being taken into consideration, the size of the eight amplitudes alternates. This indicates that low-frequency vibrational energy can be transferred among the eight intact segments through the channel of resonance coupling. As a consequence, at a given moment, the energy relatively is concentrated upon one of the intact segments, but at another instant upon one of the others. As a result of such a collective effect, the maximum displacement can be amplified up to 2.5-times in comparison to the case in which resonant coupling is absent (see Q_2 and Q_6 of fig. 22 as well as the explanation in the figure legend), and the corresponding energies therefore increased 6.25-fold. Similar results have also been obtained for the case of linear coupling [62]. Such a phenomenon, however, does not violate the law of energy conservation, since a large increase of amplitude (energy) in one intact segment occurs at the expense of a decrease of amplitudes (energies) in all others, with the total energy remaining unchanged during the entire process. Furthermore, if the number of oscillators increases, the resonant effect in magnifying the amplitude will increase accordingly, regardless of the type of coupling [62]. However, according to the law of energy conservation, the increase in amplitude cannot be greater than $\sqrt{n_p}$, where n_p is the number of intact segments involved in the resonance coupling (B. Mao et al., manuscript in preparation).

As is well known, a realistic DNA molecule generally contains more than eight intact segments, and hence the effect of increasing amplitude will be even greater than that shown in fig. 22. Consequently, the following two situations emerge: (1) the hole in the DNA might be forced to open much more widely and thereby to facilitate intercalation; (2) the hydrogen bonds, especially those close to the edges of the intact segments, will be broken when the drastic increase in amplitude exceeds the strain limit of a hydrogen bond, which is about 0.5 Å. The latter will lead to a local 'quake-like' motion.

The physical picture of quake-like motion can be described as follows: when the stress along the hydrogen bonds of base-pairs is overly built up due to the resonant effect, the dynamic equilibrium between the strain and stress will cease to exist, leading suddenly to a free jerk. The local quake-like motion is therefore the result of an excessive concentration of energy, which is caused at times by the low-frequency collective motion in DNA. After the sudden release of energy via the local quake motion, the broken hydrogen bonds will be spontaneously restored if no intercalating agent is incorporated. Such a drastic dynamic process, however short-lived it might be, will generate a zipper-gap-type hole (fig. 23), which undoubtedly provides a good chance of intercalation occurring.

The difference between the breathing and local quake-like motions is that the former is caused by random thermal collision and can only break a single base-pair within a given period of time, whereas the latter is a result of collective effects with resonance coupling and can disrupt considerably more base-pairs simultaneously.

The computer-modeling studies (fig. 24a) indicate that in order for insertion of a porphin into DNA to occur, more than five consecutive base-pairs must be open at almost the same moment, which is far

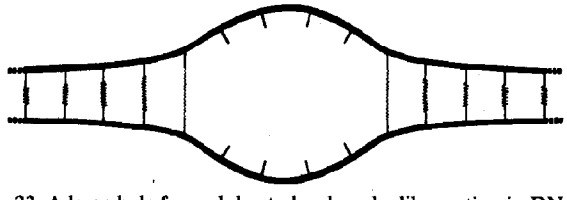

Fig. 23. A large hole formed due to local quake-like motion in DNA.

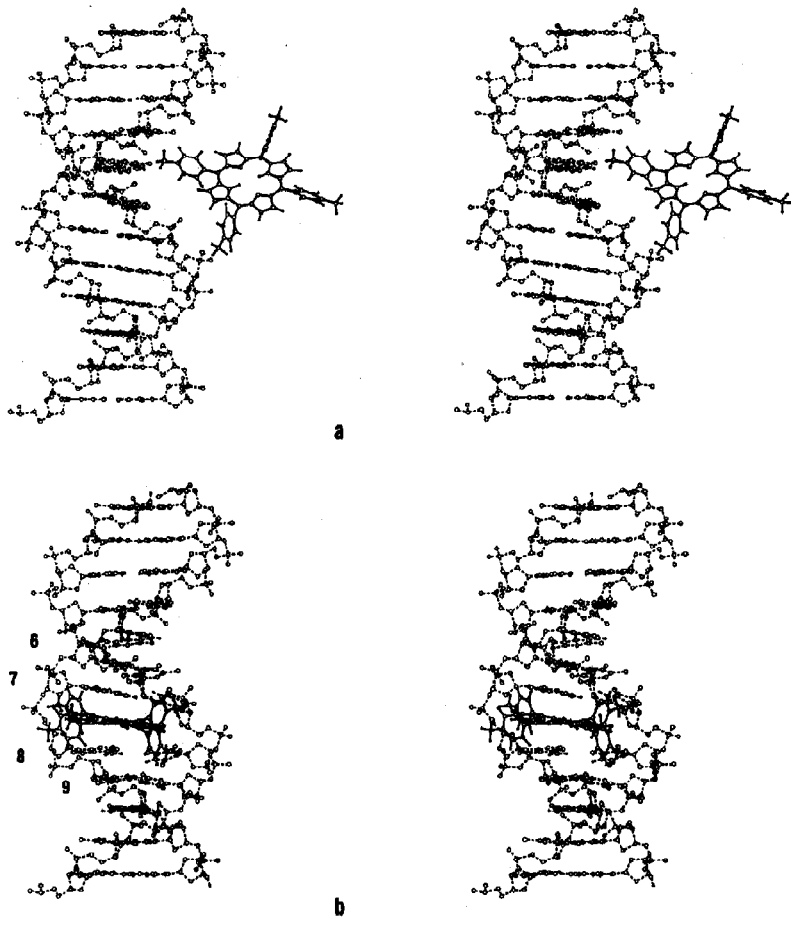

Fig. 24. Stereoscopic drawing of a segmental DNA and a drug, where DNA is represented by broken lines and the drug by continuous lines: (a) representative geometry of B-form poly(A-T)$_{12}$ DNA and porphin before intercalation; (b) conformation of the DNA-porphin complex obtained after intercalation and energy minimization. It is obvious from (a) that more than five base-pairs must be broken before a porphin can be incorporated into the DNA. After insertion of the porphin and the subsequent energy minimization (b), some of the ruptured hydrogen bonds can be reformed, however, two base-pairs remain broken (i.e., the seventh and eighth) and another two are severely distorted (i.e., the sixth and ninth). One can also see from (b) that, after intercalation and energy minimization, only the inner tetrapyrrole ring of the porphin interacts directly with the bases but that its outer pyridine rings project away from the helix axis into the grooves, as described by Fiel and Munson [60]. The AMBER force field [64] and the steepest algorithm were used for energy minimization, which was carried out after the drug molecule had been inserted into the space between the seventh and eight base-pairs of the poly(A-T)$_{12}$ DNA.

beyond the reach of normal breathing motion and can only be produced by the local quake motion. Once intercalated,the energy minimizations carried out for the DNA-porphin complex indicate that only the inner tetrapyrrole ring interacts directly with the bases (fig. 24b), as suggested by Fiel and Munson [60]. However, in contrast to their model in which it is stated that, once intercalated, the broken hydrogen bonds "can reform with only a minimal distortion of helix" [60], our energy-minimized conformation (fig. 24b) shows the disruption of two (the seventh and eighth) base-pairs, which are closest to the intercalated drug, and severe distortion of the other two (the sixth and ninth) base-pairs, which are next closest to the drug.

For smaller intercalating agents, this local quake-like motion can also provide a significant mode of entry for intercalation. This is because the normal vertical separation between base-pairs is quite small and the intercalation of even a small drug into the space between any two neighboring base-pairs will result in an obvious distortion of two to four base-pairs, as demonstrated by computer-modeling studies [62].

Therefore, the low-frequency collective motion in a DNA molecule as reflected by the dynamic picture of resonance coupling among its intact segments is the impetus for DNA molecules, irrespective of whether they are linear or circular, to accommodate intercalators, especially the larger ones.

3.4. Damping effect

What happens to energy transfer via resonance coupling if the damping effect is taken into account? Damping weakens the maximum amplitude somewhat and hence will, to a certain extent, influence the efficiency of energy transfer. Nevertheless, this does not invalidate the basic physical picture of energy transfer through the resonance-coupled channel, provided that the damping is not exceedingly large [50]. In other words, the dynamic mechanisms of energy transfer via the resonance-coupled channel remain approximately valid at least for the initial few periods. Furthermore, damping of the amplitude can always be compensated for by continuous thermal collision with solvent molecules. This is why a conspicuous low-frequency peak (corresponding to the dominant low-frequency mode) can always be observed for many protein and DNA molecules [5–9] although various extremely complicated dissipative effects certainly do exist in these molecules. Consequently, even when there is damping effect in a real system, under most circumstances both of the following basic physical features in a resonance-coupled system still hold true: (1) a significant increase in the maximum amplitude, and (2) the alternate occurrence of the maximum amplitude for each of the constituent oscillators, representing energy transfer through the channel of resonant coupling. This is the explanation for the fact that, in real life, people often experience various resonance effects in spite of the complicated nature of real environments. Therefore, the quintessence of the proposed dynamic mechanisms in sections 3.1–3.3 remains valid even though a number of complicated factors, such as the 'frictional' interaction inside a biomacromolecule [17] and the solvent viscosity, are taken into account.

4. Conclusions

One of the present-day frontiers in molecular biology is the study of low-frequency collective motions in biological macromolecules and the relevant biological functions.The origins of this kind of internal motion are: (1) the presence of a series of weak bonds, such as hydrogen bonds and salt bridges, in biological macromolecules, and (2) large numbers of atoms are distributed around those weak bonds.

Based on the conception of such an origin, the quasi-continuity model has been developed, by which we can successfully calculate the dominant low-frequency motion in a biomacromolecule.

The so-called dominant low-frequency mode is that which corresponds to the maximum low-frequency peak observed for a biomacromolecule. In addition, such a low frequency can also be termed the activating low-frequency mode, since it is closely related to the activation and deactivation of that biomolecule. From a physical point of view, the dominant low-frequency mode represents a particular kind of internal collective movement in a biomacromolecule and hence involves substantial numbers of atoms therein, as described by the quasi-continuity model. Due to various favorable factors, the number of phonons excited with this exceptional mode is overwhelmingly large in comparison with the other modes possible. From a biological point of view, the dominant low-frequency motion plays a significantly greater role than other modes because it spans a larger space and involves a greater displacement, especially with respect to signal transmission, such as occurs for allosteric transitions and the cooperative effect.

The biological functions of low-frequency motion can be classified into two categories as follows:

4.1. Thermodynamic aspect

Within the frequency spectrum of a biomacromolecule, only the low-frequency portion (of wave numbers less than 50 cm^{-1}) can contribute significant phonon entropy and hence plays an important role in the association of biomacromolecules. As an example, it was demonstrated that associations between insulin and the insulin receptor as well as insulin and insulin antibody would simultaneously excite low-frequency phonons (of wave numbers in the range 10–50 cm^{-1}), otherwise the free energy could not be balanced and a thermodynamic 'deficit' would occur.

4.2. Dynamic aspect

The low-frequency internal motion of a biomacromolecule is closely related to its biological activity, as reflected in the fact that, not only is the loss of its activity always accompanied by the disappearance of its dominant low-frequency peak, but also that the low-frequency internal motion seems indispensable to our understanding of the various marvellous biological functions manifested in many biomacromolecules. For example, the cooperativity of hemoglobin, the chelate and trigger effects for antibodies, as well as the intercalation between DNA and drugs, whose dynamic mechanisms had long been too complicated and difficult to elucidate, can be effectively approached by introducing the conception of low-frequency resonant coupling.

Appendix A. Derivation of eq. 38

Suppose q_i is the vibrational displacement of the i-th rod from its equilibrium position (fig. 7). We then have

$$\begin{aligned} m\ddot{q}_1 &= -\lambda k_H^{\beta}(q_1 - q_2) \\ m\ddot{q}_l &= -\lambda k_H^{\beta}(q_l - q_{l-1}) - \lambda k_H^{\beta}(q_l - q_{l+1}) \\ (l &= 2, 3, \ldots, \mu - 1) \\ m\ddot{q}_\mu &= -\lambda k_H^{\beta}(q_\mu - q_{\mu-1}) \end{aligned} \tag{A1}$$

where m, λ, k_H^{β} and μ have already been defined in the text. Substituting

$$q_i = C_i \cos(\omega t + \phi) \tag{A2}$$

into eq. A1, we obtain

The μ-th column

The μ-th row

$$\begin{bmatrix} x-1 & -1 & & & & & \\ -1 & x & -1 & & & & \\ & -1 & x & -1 & & & \\ & & \ddots & \ddots & \ddots & & \\ & & & -1 & x & -1 & \\ & & & & -1 & x-1 & \end{bmatrix} \begin{bmatrix} C_1 \\ C_2 \\ C_3 \\ \vdots \\ C_{\mu-1} \\ C_\mu \end{bmatrix} = 0 \tag{A3}$$

where

$$x = \frac{2\lambda k/m - \omega^2}{\lambda k/m} \tag{A4}$$

The non-trivial solution of eq. A3 requires

$$G_\mu(x) = \begin{bmatrix} x-1 & -1 & & & & \\ -1 & x & -1 & & & \\ & \ddots & \ddots & \ddots & & \\ & & -1 & x & -1 & \\ & & & -1 & x-1 \end{bmatrix} = 0 \tag{A5}$$

According to the operational regulation of a determinant, we have

$$G_\mu(x) = (x-1)^2 g_{\mu-2}(x) - 2(x-1) g_{\mu-3}(x) + g_{\mu-4}(x) \tag{A6}$$

where

$$g_m(x) = \text{The } m\text{-th row} \begin{bmatrix} x & -1 & & & \text{The } m\text{-th column} \\ -1 & x & -1 & & \\ & \ddots & \ddots & \ddots & \\ & & -1 & x & -1 \\ & & & -1 & x \end{bmatrix} \tag{A7}$$

We now observe that $g_m(x)$ possesses the following two exceptional properties (eqs. A8 and A10), which are very useful:

$$g_m(x) = x g_{m-1}(x) - g_{m-2}(x) \tag{A8}$$

the above recurrence formula can be easily proved by merely expanding the first row of the determinant in eq. A7.

If we put

$$x = 2\cos\theta \tag{A9}$$

we then obtain

$$g_m(2\cos\theta) = \frac{\sin(m+1)\theta}{\sin\theta} \tag{A10}$$

The above equation can be proved as follows. When $m = 1$ and 2, it is very easy to confirm with the use of eq. A7 that eq. A10 is correct. Now suppose that when $m = l$ and $l+1$ eq. A10 holds, then according to the recurrence formula, eq. A8, we have

$$g_{l+2}(2\cos\theta) = 2\cos\theta\, g_{l+1}(2\cos\theta) - g_l(\cos\theta) = \frac{2\cos\theta\sin(l+2)\theta}{\sin\theta} - \frac{\sin(l+1)\theta}{\sin\theta} = \frac{\sin(l+3)\theta}{\sin\theta} \tag{A11}$$

The above indicates that if, when $m = l$ and $l+1$, eq. A8 holds, then it must also hold true when $m = l+2$. Consequently, eq. A10 has been generally proved by induction.

By means of eq. A8, eq. A6 can be reduced to

$$G_\mu(x) = g_\mu(x) + g_{\mu-2}(x) - 2g_{\mu-1}(x) \tag{A13}$$

Then, using eqs. A9 and A10, the above can be further reduced to

$$G_\mu(2\cos\theta) = \frac{2\sin\mu\theta(\cos\theta - 1)}{\sin\theta} \tag{A14}$$

From eq. A14 one can observe that $G_\mu(2\cos\theta) = 0$ when $\theta = l\pi/\mu$ $(l = 1, 2, \ldots, n-1)$. Moreover, using l'Hospital's rule, we can find G_μ $(2\cos\theta) = 0$ even when $\theta = 0$. Therefore, the μ roots of eq. A5 are

$$\begin{aligned} &x_l = 2\cos\theta_l = 2\cos(l\pi/\mu) \\ &(l = 0, 1, 2, \ldots, \mu - 1) \end{aligned} \tag{A15}$$

Substituting eq. A15 into eq. A4, we obtain

$$\begin{aligned} &\omega_l = \sqrt{2[1 - \cos(l\pi/n)]\,\frac{\lambda k_{\mathrm{H}}^{\beta}}{m}} \\ &(l = 0, 1, 2, \ldots, \mu - 1) \end{aligned} \tag{A16}$$

When $l = 0$ we always have $\omega_0 = 0$, indicating that the corresponding motion is translational rather than vibrational. When $l = 1$, however, the normal mode has the nature of accordion-like motion as will be shown later. In this case, we have

$$\omega = \omega_1 = \sqrt{2[1 - \cos(\pi/n)]\left(\lambda k_{\mathrm{H}}^{\beta}/m\right)} \tag{A17}$$

so that the lowest-frequency wave number should be

$$\tilde{\nu} = \frac{\omega}{2\pi c} = \frac{1}{\pi c}\sqrt{[1 - \cos(\pi/n)]\left(\lambda k_{\mathrm{H}}^{\beta}/2m\right)} \tag{A18}$$

Furthermore, according to eq. A3, the corresponding amplitude coefficients are

$$\begin{aligned} &C_1^l = A \\ &C_2^l = [2\cos(l\pi/n) - 1]\,C_1^l \\ &C_i^l = 2\cos(l\pi/n)C_{i-1}^l - C_{i-2}^l \\ &(i = 3, \ldots, n) \end{aligned} \tag{A19}$$

For example, when $n = 6$, for the lowest-frequency mode we have

$$\begin{bmatrix} C_1^1 \\ C_2^1 \\ C_3^1 \\ C_4^1 \\ C_5^1 \\ C_6^1 \end{bmatrix} = \begin{bmatrix} 1 \\ \sqrt{3} - 1 \\ 2 - \sqrt{3} \\ \sqrt{3} - 2 \\ 1 - \sqrt{3} \\ -1 \end{bmatrix} A = \begin{bmatrix} 1 \\ \sqrt{3} - 1 \\ 2 - \sqrt{3} \\ -(2 - \sqrt{3}) \\ -(\sqrt{3} - 1) \\ -1 \end{bmatrix} A \tag{A20}$$

The above indicates that the lowest-frequency mode carries out accordion-like motion.

Acknowledgements

Invaluable discussions with Dr. G.M. Maggiora, Dr. B. Mao, and Dr. C.T. Goodhue are gratefully acknowledged.

References

1 C.R. Kahn, P. Freychet and J. Roth, J. Biol. Chem. 249 (1974) 2249.
2 K.C. Chou and N.Y. Chen, Sci. Sin. 20 (1977) 447.
3 C. Chothia and J. Janin, Nature 256 (1975) 705.
4 L.D. Landau and E.M. Lifshitz, Statistical Physics, part 1, (Pergamon Press, Oxford, 1985) p. 71.
5 K.G. Brown, S.C. Erfurth, E.W. Small and W.L. Peticolas, Proc. Natl. Acad. Sci. U.S.A. 69 (1972) 1467.
6 L. Genzel, F. Keilman, T.P. Martin, G. Winterling, Y. Yacoby, H. Fröhlich and M.W. Makinen, Biopolymers 15 (1976) 219.
7 P.C. Painter and L.E. Mosher, Biopolymers 18 (1979) 3121.
8 P.C. Painter, L.E. Mosher and C. Rhoads, Biopolymers 20 (1981) 243.
9 P.C. Painter, L.E. Mosher and C. Rhoads, Biopolymers 21 (1982) 1469.
10 Y. Suezaki and N. Gō, Int. J. Peptide Protein Res. 7 (1975) 333.
11 T. Noguti and N. Gō, Nature 296 (1982) 776.
12 N. Gō, T. Noguti and T. Nishikawa, Proc. Natl. Acad. Sci. U.S.A. 80 (1983) 3696.
13 B. Brooks and M. Karplus, Proc. Natl. Acad. Sci. U.S.A. 80 (1982) 6571.
14 R.M. Levy, A.R. Srinivasam, W.K. Olson and J.A. McCammon, Biopolymers 23 (1984) 1099.
15 K.C. Chou, Biochem. J. 215 (1983) 465.
16 K.C. Chou, Biophys. J. 45 (1984) 881.
17 K.C. Chou, Biochem. J. 209 (1983) 573.
18 K.C. Chou, Biophys. J. 48 (1985) 289.
19 K.C. Chou, Biochem. J. 221 (1984) 27.
20 K.C. Chou, Biophys. Chem. 25 (1986) 105.
21 B. Mao and A.J. McCammon, J. Biol. Chem. 258 (1983) 12543.
22 K.C. Chou, G. Némethy and H.A. Scheraga, J. Phys. Chem. 87 (1983) 2869.
23 K. Itoh and T. Shimanouchi, Biopolymers 9 (1970) 383.
24 T. Blundell, G. Dodson, D. Hodgkin and D. Mercola, Adv. Protein Chem. 26 (1972) 279.
25 K.C. Chou, G. Némethy and H.A. Scheraga, J. Mol. Biol. 168 (1983) 389.
26 M.J.E. Sternberg and J.M. Thornton, J. Mol. Biol. 110 (1977) 285.
27 K.C. Chou, M. Pottle, G. Némethy, Y. Ueda and H.A. Scheraga, J. Mol. Biol. 162 (1982) 89.
28 W.G.J. Hol, L.M. Halie and C. Sander, Nature 294 (1981) 532.
29 S. Lifson and C. Sander, Nature 282 (1979) 109.
30 C. Chothia, J. Mol. Biol. 75 (1973) 295.
31 J.S. Richardson, Adv. Protein Chem. 34 (1981) 167.
32 F.C. Bernstein, T.F. Koetzle, G.J.B. Williams, E.F. Meyer, Jr, M.D. Brice, J.R. Rodgers, O. Kennard, T. Shimanouchi and M. Tasumi, J. Mol. Biol. 112 (1977) 535.
33 G.N. Reeke, Jr, J.W. Becker and G.M. Edelman, J. Biol. Chem. 250 (1975) 1525.
34 G.S. Manning, Biopolymers 22 (1983) 689.
35 C. Mandal, N.R. Kallenbach and S.W. Englander, J. Mol. Biol. 135 (1979) 391.
36 G. Careri, P. Fasella and E. Grartton, CRC Crit. Rev. Biochem. 3 (1975) 141.
37 K.C. Chou, Biopolymers 26 (1987) 285.
38 R.C. Bohinski, Modern concepts in biochemistry, 2nd edn. (Allyn and Bacon, Boston, 1976) ch. 7.
39 M.F. Perutz, Proc. Roy. Soc. B173 (1969) 113.
40 T.R. Lindstrom and C. Ho, Proc. Natl. Acad. Sci. U.S.A. 69 (1972) 1707.
41 R.D. Gray and Q.H. Gibson, J. Biol. Chem. 246 (1971) 5176.
42 K.C. Chou, N.Y. Chen and S. Forsén, Chem. Scr. 18 (1981) 126.
43 K.C. Chou, Biophys. Chem. 20 (1984) 61.
44 K.S. Suslick and T.J. Reinert, J. Chem. Educ. 62 (1985) 974.
45 D. Beale and A. Feinstein, Q. Rev. Biophys. 9 (1976) 135.
46 D.R. Davies, E.A. Padlan and D.M. Segal, Annu. Rev. Biochem. 44 (1975) 639.
47 E.A. Padlan, Q. Rev. Biophys. 10 (1977) 35.

48 D.A.D. Parry and E.N. Baker, Rep. Prog. Phys. 47 (1984) 1133.
49 F.A. Saul, L.M. Amzel and R.J. Poljak, J. Biol. Chem. 253 (1978) 585.
50 K.C. Chou and Y.S. Kiang, Biophys. Chem. 22 (1985) 219.
51 C.R. Cantor and P.R. Schimmel, Biophysical chemistry (W.H. Freeman, San Francisco, 1980) ch. 1, p. 22.
52 J. Schlessinger, I.Z. Steinberg, D. Givol, J. Hochman and I. Pecht, Proc. Natl. Acad. Sci. U.S.A. 72 (1975) 2775.
53 I. Pecht, B. Ehrenberg, E. Calef, and R. Arnon, Biochem. Biophys. Res. Commun. 74 (1977) 1302.
54 P.H. Schur and G.D. Christian, J. Exp. Med. 120 (1964) 531.
55 K.C. Chou and S.P. Jiang, Sci. Sin. 17 (1974) 664.
56 K.C. Chou, Sci. Sin. 19 (1976) 505.
57 G. Zhou, M.T. Wong and G.P. Zhou, Biophys. Chem. 18 (1983) 125.
58 G.P. Zhou, T.T. Li and K.C. Chou, Biophys. Chem. 14 (1981) 277.
59 H.M. Sobell, in: Structures of biological macromolecules and assemblies, eds. F. Jurnak and A. McPherson (Wiley, New York, 1985) vol. 2, p. 172.
60 R.J. Fiel and B.R. Munson, Nucleic Acids Res. 8 (1980) 2835.
61 K.C. Chou and G.M. Maggiora, Br. Polym. J. (1988) in the press.
62 K.C. Chou and B. Mao, to be published.
63 P.A.W. Lewis, A.S. Goodman, and J.M. Miller, IBM Syst. J. 8 (1969) 136.
64 P.K. Weiner and P.A. Kollman, J. Comp. Chem. 2 (1981) 287.